Ordered Mesoporous Alumina with Tunable Morphologies and Pore Sizes for CO_2 Capture and Dye Separation

Geok Leng Seah,[†,⊥] Leyan Wang,[†,⊥] Li Fang Tan,[†] Chanikarn Tipjanrawee,[†] Wardhana A. Sasangka,[†] Adam K. Usadi,[‡] Jonathan M. McConnachie,[‡] and Kwan W. Tan[†,]*

[†]School of Materials Science and Engineering, Nanyang Technological University, Singapore 639798, Singapore.

[‡]ExxonMobil Research and Engineering Company, Annandale, New Jersey 08801, United States.

[⊥]These authors contributed equally to the work.

[*]Address correspondence to kwtan@ntu.edu.sg.

Keywords: ordered alumina, mesoporous, hierarchical structures, self-assembly, block copolymers, scalability; CO_2 capture, dye separation

ABSTRACT

We describe a versatile and scalable strategy towards long-range and periodically ordered mesoporous alumina (Al_2O_3) structures by evaporation-induced self-assembly of structure-directing ABA triblock copolymer (F127) mixed with aluminum tri-*sec*-butoxide–derived sol additive. We found that separate preparation of the alkoxide sol-gel reaction before mixing with the block copolymer enabled access to a relatively unexplored parameter space of copolymer-to-additive composition, acid-to-metal molar ratio and solvent, yielding ordered mesophases of two-dimensional (2D) lamellar, hexagonal cylinder and 3D cage-like cubic lattices, as well as multiscale hierarchical ordered structures from spinodal decomposition-induced macro- and mesophase separation. Thermal annealing in air at 900 °C yielded well-ordered mesoporous crystalline γ-Al_2O_3 structures and hierarchically porous γ-Al_2O_3 with 3D interconnected macroscale and ordered mesoscale pore networks. The ordered Al_2O_3 structures exhibited tunable pore sizes in three different length scales, <2 nm (micropore), 2-11 nm (mesopore) and 1-5 μm (macropore), as well as high surface areas and pore volumes up to 305 m^2/g and 0.33 cm^3/g, respectively. Moreover, the resultant mesoporous Al_2O_3 demonstrated enhanced adsorption capacities of carbon dioxide and Congo red dye. Such hierarchically ordered mesoporous Al_2O_3 are well-suited for green environmental solutions and urban sustainability applications, for example, high-temperature solid adsorbents and catalyst supports for carbon dioxide sequestration, fuel cells and wastewater separation treatments.

INTRODUCTION

Mesoporous alumina (Al_2O_3) materials with high chemical, mechanical and thermal stability have been widely adapted in many industrial applications such as high-temperature catalysis and adsorption.[1–3] Improving mesoporous Al_2O_3 with structural and textural features such as periodicity and long range order, uniform pore size and good connectivity, high surface area and pore volume, acidic/basic surface characteristics and addition of metal components, can further enhance their physical and chemical functionalities and expand the application space into energy conversion, size-selective separation and sensing of environmental pollutants, as well as enrichment of biomacromolecules.[3–17]

Self-assembly of surfactant and block copolymers (BCPs) as structure-directing agents (SDAs) for molecular organic and sol-gel derived inorganic precursors is a well-established soft-templating pathway towards well-ordered mesoporous carbon, silica and metal oxide structures.[15,18–25] In particular, Niesz *et al.*, Yuan *et al.* and Tan *et al.* showed coupling self-assembling polyethylene oxide-*block*-polypropylene oxide-*block*-polyethylene oxide (PEO-*b*-PPO-*b*-PEO, e.g., F127 and P123) and polyisoprene-*block*-polystyrene-*block*-polyethylene oxide (PI-*b*-PS-*b*-PEO) BCPs with Al_2O_3 sol-derived additives formed under controlled hydrolysis rates, yielded highly ordered mesoporous Al_2O_3 with hexagonally arranged channels (*p6mm*).[5,6,15] However, the compositional parameter space for alternative morphologies remains limited. For example, Grant *et al.* observed a poorly defined cage-like body-centered cubic ($Im\bar{3}m$) mesophase under a highly specific combination of F127/Al_2O_3 composition and ethanol volume.[26] They further observed higher nitric acid/metal ratios promoted mesophase transition of hexagonal to unspecified cage-like cubic morphologies in the P123–Al_2O_3 system.[27] Small-angle X-ray scattering data indicated loss of long-range order for some cubic mesostructures after

thermal annealing at 900 °C.[26,27] In a separate work, Wei *et al.* observed a single mesophase of face-centered cubic ($Fm\bar{3}m$) lattice in mesoporous Al_2O_3 thin films using polystyrene-*block*-polyethylene oxide (PS-*b*-PEO) as SDA and pre-stabilized Al_2O_3 nanoparticles as additive.[11] Even as minor variations of BCP/Al_2O_3 composition and acid/Al ratios typically resulted in structural disorder and macroscopic phase separation,[5,26,27] facile access to other complex self-organized Al_2O_3 mesostructures via BCP soft-templating remains highly desirable. And while mesoporous Al_2O_3 structures of other morphologies and pore sizes can be obtained using ordered hard templates, the process requires multiple synthesis steps such as template preparation and backfilling of precursors, thereby increasing both time and cost.[3,28,29]

Here we report a systematic study of the mesophase ordering of a family of long-range and periodically ordered Al_2O_3 structures generated by the evaporation-induced self-assembly (EISA) of commercially available PEO-*b*-PPO-*b*-PEO tri-BCP (F127) as SDA, aluminum tri-*sec*-butoxide ($Al(O^sBu)_3$) as source of Al_2O_3 and nitric acid (HNO_3) as catalyst. In particular, separate preparation of the HNO_3-catalysed sol-gel reaction of $Al(O^sBu)_3$ to form stable Al_2O_3 sol precursors followed by adding into the ethanolic solution of F127 SDA, facilitates the co-assembly process. The mesophase family members of 2D lamellar, hexagonal ($p6mm$) and 3D cage-like cubic ($Im\bar{3}m$) lattices, as well as hierarchical structures with 3D interconnected macroscale and hexagonally arranged mesoscale pore networks, can be reproducibly synthesized. To the best of our knowledge, observations of the lamellar lattice and hierarchically ordered mesoporous Al_2O_3 are reported for the first time. The formation pathways for lyotropic liquid crystalline-like mesophase transitions in F127–Al_2O_3 monoliths via variations of the F127/Al_2O_3 compositions (17–39 wt% Al_2O_3), HNO_3/Al molar ratios (1.2–2.0), and solvents for sol–gel reaction of $Al(O^sBu)_3$, are elucidated and presented in a two-component morphology map. The

hybrid composites transformed into highly crystalline mesoporous γ-Al_2O_3 and retained their long-range order after thermal annealing in air at 900 °C. Finally, the resultant mesoporous ordered Al_2O_3 structures exhibited excellent adsorption capacities and affinities for carbon dioxide and Congo red dye molecules compared to commercial Al_2O_3 material.

EXPERIMENTAL SECTION

Materials. All chemicals were used as received. Pluronic F127 (PEO-*b*-PPO-*b*-PEO, 12.6 kg/mol), aluminum tri-*sec*-butoxide ($Al(O^sBu)_3$), 97%), *n*-butanol (*n*-BuOH, anhydrous 99.8%), commercial Al_2O_3 (A1522, Type WN-6, Neutral, Activity Grade Super I) and Congo Red (≥85%) were obtained from Sigma-Aldrich. Absolute ethanol (EtOH, 200 proof) was obtained from Merck. Nitric acid (HNO_3, 69 wt% in water) was obtained from Honeywell International.

Synthesis of F127–Al_2O_3 Hybrid Monoliths (HNO_3/Al = 2). In a typical synthesis, a 10 wt% F127 solution was prepared by dissolving 10 g of F127 in 90 g of EtOH at 40 °C in a reagent bottle. In a separate scintillation vial, 3.76 g (81.7 mmol) of EtOH was added to 1 g (4.0 mmol) of $Al(O^sBu)_3$ and left undisturbed for 30 min, followed by vigorous stirring for another 30 min, forming a white cloudy suspension due to alcoholysis reaction.[15,30] 0.526 mL (8.1 mmol) of HNO_3 was carefully added into the cloudy mixture and stirred vigorously for 6 h to obtain a colorless transparent Al_2O_3 sol solution under ambient conditions. The water source for hydrolysis of $Al(O^sBu)_3$ was HNO_3 acid. The molar ratios of HNO_3/Al and H_2O/Al in the EtOH-based Al_2O_3 sol mother solution were approximately 2:1 and 3:1, respectively. Appropriate aliquots of Al_2O_3 sol solution were then mixed with the 10 wt% F127 solution to obtain hybrid samples of varying F127/Al_2O_3 compositions. For example, 1.58 g aliquot of Al_2O_3 sol solution (18.2 wt% $Al(O^sBu)_3$) was added to 1.80 g of 10 wt% F127 solution to obtain a hybrid

composite comprising a theoretical composition of 25 wt% Al_2O_3. The actual value obtained from thermogravimetric analysis was 23 wt% Al_2O_3, indicating close agreement with our calculations. The final composition of the hybrid samples ranged from 17 to 39 wt% Al_2O_3 (Figure S1).

The colorless transparent F127–Al_2O_3 hybrid solutions were stirred for 30 min and then cast in 5 mL (1.7 cm diameter) and 10 mL (2.1 cm diameter) PTFE beakers set on a glass Petri dish covered with hemispherical glass dome, and heated at 50 °C for EISA over 3–7 days under ambient conditions. For scale-up experiments, the F127–Al_2O_3 hybrid solutions were cast in crystallization dishes of 5 cm and 7.5 cm diameters. Typically, six 1.7-cm PTFE beakers were placed under each glass dome for EISA. To enable deeper quench depth in the spinodal decomposition regime via faster solvent evaporation rate (MA28-2-DQ), a single PTFE beaker was cast under the dome at 50 °C. It is expected that ethanol would evaporate at a faster rate with the reduction of overall ethanol vapor pressure in the dome. The hybrid monolithic samples were cured in a vacuum oven at 25 °C (20 min), 40 °C (50 min), 60 °C (>12 h), 100 °C (2 h) and finally 130 °C (2 h).

F127–Al_2O_3 Hybrids of Varying HNO_3/Al Molar Ratios. New hybrid samples with different HNO_3/Al molar ratios of 1.2–1.8 were synthesized by preparing different Al_2O_3 sol mother solutions in EtOH. The inorganic composition was maintained at 23 wt% Al_2O_3 for all samples.

For the Al_2O_3 sol solution with HNO_3/Al molar ratio of 1.6, 3.76 g (81.7 mmol) of EtOH was added to 1 g (4.0 mmol) of $Al(O^sBu)_3$ and left undisturbed for 30 min, followed by vigorous stirring for another 30 min, forming a white cloudy suspension. 0.421 mL (6.5 mmol) of HNO_3 was carefully added into the cloudy mixture and stirred vigorously for 12 h to obtain a colorless

transparent Al_2O_3 sol solution under ambient conditions. A 1.53 g aliquot (18.7 wt% $Al(O^sBu)_3$) was then added into a 1.80 g 10 wt% F127 solution, followed by EISA and thermal curing as described above.

For other Al_2O_3 sol solutions, 0.316, 0.368, and 0.473 mL of HNO_3 were added into the $Al(O^sBu)_3$–EtOH mixtures in separate vials and stirred for different durations to obtain colorless transparent solutions with HNO_3/Al molar ratios of 1.2 (60 h), 1.4 (36 h), and 1.8 (12 h), respectively.

***n*-BuOH for Hydrolysis and Condensation of $Al(O^sBu)_3$.** New hybrid samples were synthesized using BuOH-based Al_2O_3 sol additive. The BuOH-based additive was prepared by adding 3.76 g (50.8 mmol) of *n*-BuOH to 1 g (4.0 mmol) of $Al(O^sBu)_3$ and left undisturbed for 30 min, followed by vigorous stirring for another 30 min, forming a white cloudy suspension. 0.421 mL (6.5 mmol) of HNO_3 was added into the cloudy mixture and stirred vigorously for 12 h to obtain a colorless transparent BuOH-based Al_2O_3 sol solution. A 1.53 g (18.7 wt% $Al(O^sBu)_3$)) aliquot was then added into a 1.80 g 10 wt% F127 solution, followed by EISA and thermal curing as described above, to obtain hybrid samples comprising 23 wt% Al_2O_3 (HNO_3/Al = 1.6).

Mesoporous Al_2O_3 Monoliths. The F127–Al_2O_3 hybrids were heated in a tube furnace under static air at 450–1000 °C (3 h) for polymer removal and Al_2O_3 crystallization, with a ramp rate of 1 °C/min.

Carbon Dioxide Adsorption Experiments. Carbon dioxide sorption measurements were conducted using a Micromeritics ASAP 2020 at 0 °C and 25 °C. Samples were degassed at

130 °C overnight under vacuum before measurement. The density of carbon dioxide at 0 and 25 °C are 1.951 and 1.784 kg/m^3, respectively.

Congo Red Adsorption Experiments. All adsorption experiments were performed in the dark to prevent photobleaching of Congo red dye. 10 mg of finely powdered mesoporous Al_2O_3 samples were dispersed in a 70 mL aqueous Congo red solution (50 mg/L) under continuous stirring at 750 rpm. At a specific time point, an aliquot of 2 mL was extracted from the Al_2O_3–Congo red mixture and separated by centrifugation at 5000 rpm for 10 min. The supernatant with remaining Congo red dye was then collected for UV-vis absorbance measurement. A calibration curve was obtained by measuring the absorbance of aqueous Congo red solutions for the concentration range of 1 to 50 mg/L at at λ_{max} = 498 nm. It is noted that Congo red was added in excess for all mesoporous Al_2O_3 samples, i.e., 3.5 mg of dye per 10 mg of Al_2O_3.

Characterization. Small-angle X-ray scattering (SAXS) measurements were collected with a Xenocs Nano-inXider using Cu K_α radiation source and Dectris Pilatus 3 detectors. Using the Xenocs FOXTROT software, 2D SAXS patterns were azimuthally integrated around the beam center into 1D scattering intensity curves plotted against the scattering vector magnitude $q = 4\pi \sin\theta/\lambda$, where θ is half of the total scattering angle and λ is the X-ray wavelength. The cylinder-to-cylinder distance of *p6mm* lattice was calculated using $d = 4\pi/\left(\sqrt{3}q^*\right)$, where q^* is the scattering vector of the principal peak. The *d*-spacing for lamellar and disordered structures was calculated using $d = 2\pi/q^*$. Scattering vector of the principal reflection of $Im\bar{3}m$ lattice was calculated from $q^* = 2\pi/d_{110}$, where d_{110} is the interplanar distance of (110) plane.[24] Powder X-ray diffraction (PXRD) data were collected with a Bruker D8 Advanced XRD instrument using Cu K_α radiation.

Transmission electron micrographs (TEM) were obtained using the JEOL 2010 and 2100F electron microscopes operating at the accelerating voltage of 200 kV equipped with the AMT XR40B CCD camera and Gatan Ultrascan 1000XP CCD camera, respectively. Scanning electron micrographs (SEM) were collected on Pt-coated mesoporous Al_2O_3 samples using a JEOL 7600F field emission scanning electron microscope equipped with a half-in-lens detector.

Nitrogen sorption measurements were conducted using a Micromeritics ASAP 2020 at −196 °C. Samples were degassed at 130 ℃ overnight under vacuum before measurement. The specific surface areas were obtained using the Brunauer–Emmett–Teller (BET) method below 0.2 P/P_0.[31] The mesopore size distributions were obtained by the Barret–Joyner–Halenda (BJH) method together with the improved Kruk–Jaroniec–Sayari (KJS) model using the adsorption branch of nitrogen isotherms.[32,33] The micropore size distributions were obtained using the *t*-plot method.[34] Single point adsorption pore volumes were extracted at 0.99 P/P_0.

Thermogravimetric analysis (TGA) measurements were conducted using a TA Instruments Q500 in air with a heating rate of 10 ℃/min. UV-vis spectroscopy measurements were collected using a Shimazu UV-vis spectrometer UV2700 in the dark under ambient conditions.

RESULTS AND DISCUSSION

Influence of Composition on Ordered Mesoporous F127–Al_2O_3 Monoliths. In some earlier works, Al precursors and acid catalysts were typically added into the BCP solutions within short intervals (≤15 min), leading to the occurrence of multiple simultaneous reactions (e.g., alcoholysis, Al_2O_3 sol–gel hydrolysis/condensation reactions) in the mixtures.[5,6,26,27,35,36]

However, the tumultuous chain of reactions may cause the weakening of interactions between organic-inorganic components and impede mesophase ordering, especially under higher BCP/Al_2O_3 compositions and/or HNO_3/Al ratios.[23,35,37] To this end, we decoupled the hydrolysis/condensation reactions of $Al(O^sBu)_3$ into Al_2O_3 sol additive in a separate vial before mixing with the F127 BCP solution, thereby introducing an additional level of control to access more complex morphologies.

Figure 1 shows the synthesis route schematic towards periodically ordered F127-directed mesoporous Al_2O_3 structures. First in a separate vial, $Al(O^sBu)_3$ was added into EtOH, triggering the exchange of *sec*-butoxy with ethoxy ligands surrounding the Al^{3+} cation (alcoholysis).[15,30,35] HNO_3 (69 wt%) was then added as the catalyst and water source for the hydrolysis of $Al(O^sBu)_3$. As an example, the molar ratio of HNO_3/Al of the sol mixture was first set at 2:1 to obtain a transparent colorless solution of Al_2O_3 sol oligomers (or hydrophilic nanoclusters) in EtOH.[6,37,38] Aliquots of different amounts of Al_2O_3 sol additive were mixed with F127 BCP dissolved in EtOH, enabling selective interactions of metal oxide sol to the hydrophilic PEO-corona of F127 micelles by hydrogen bonding.[5,6,15,21,22] The resultant hybrid solutions were then cast in PTFE beakers for EISA and thermal curing to form monoliths of various periodically ordered F127–Al_2O_3 mesostructures (Figure S2). Thermal annealing in air up to 900 °C removed the BCP and yielded long-range ordered crystalline mesoporous Al_2O_3 structures.

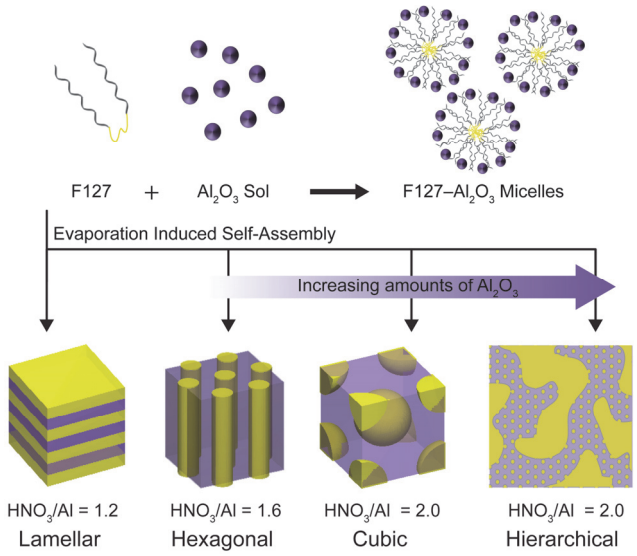

Figure 1. Schematic for EISA of periodically ordered F127–Al_2O_3 mesostructures by varying the F127/Al_2O_3 composition and HNO_3/Al molar ratio.

Figure 2 shows the SAXS patterns of hybrid and corresponding mesoporous Al_2O_3 samples as a function of increasing inorganic composition for the HNO_3/Al molar ratio of 2. Hereinafter, samples are denoted as MA*X*-*Y*-*Z*, where *X*, *Y* and *Z* indicate the Al_2O_3 composition (17 to 39 wt% Al_2O_3), HNO_3/Al molar ratio (1.2 to 2) and thermal annealing temperature (450 to 1000 °C), respectively. From Figure 2a the SAXS pattern of hybrid MA17-2 (sample (i)) exhibits a relatively broad principal peak with low intensity, suggesting a disordered mesostructure. As inorganic content increased, the SAXS patterns of hybrid MA19-2 to MA28-2 samples (samples (ii)–(vi)) show significantly improved reflections with high intensities, indicating formation of long-range ordered lattices. The principal peak (q^*) and higher-order SAXS reflections of hybrid MA19 and MA20 (samples (ii), (iii)) located at the angular positions of $(q/q^*)^2 = 1, 3, 4$, are consistent with the hexagonal cylindrical morphology (*p6mm*). While SAXS patterns of hybrid MA23-2, MA26-2 and MA28-2 (samples (iv)–(vi)) allow assignment of the *p6mm* symmetry, the shoulder featured on the right hand side of the respective principal

peak in the SAXS curves suggest a second mesophase.[39,40] The hybrid samples were likely near the boundaries of two different lattices resulting in mixed morphologies.[39,40] Finally the low intensity and lack of higher-order reflections in the SAXS pattern of hybrid MA39-2 similarly indicate a disordered structure (sample (vii)). The respective principal peak (q^*) and corresponding lattice *d*-spacing values are summarized in Table 1.

To verify the periodic lattices, hybrid samples were thermally annealed in air at 450 °C for SAXS (Figure 2b) and TEM (Figure 3) characterization. Figure 2b shows that the respective principal peak and higher-order SAXS reflections of long-range ordered mesoporous Al_2O_3 were retained after thermal annealing (samples (ii)–(vi)), albeit with some peak broadening and shift to higher *q* values ascribed to thermal-induced mesostructure shrinkage and polymer decomposition forming the pores. The overall mesoscale shrinkage is approximately 35–40%. SAXS data show that samples lacking periodic order, e.g., MA17-2-450, underwent mesostructure collapse as indicated by the disappearance of the principal peak (sample (i) in Figure 2b). TEM micrographs of MA17-2-450 (Figure 3a and S3a) show tubular/wormlike type structures, suggesting the Al_2O_3 composition of 17 wt% was insufficient to stabilize the mesophase for heat treatment. As the Al_2O_3 composition increased to 19 wt%, SAXS indicates MA19-2-450 retained the *p6mm* symmetry (sample (ii) in Figure 2b). This was corroborated by TEM showing the projection of lying-down cylinders in the direction perpendicular to hexagonally arranged mesopores (Figure 3b). As the TEM image shows a projection of wide channel lines,[41] we used the measured center-to-center distance of 10.6 nm to calculate the cylinder-to-cylinder *d*-spacing value of 12.2 nm. From SAXS the cylinder-to-cylinder *d*-spacing is found to be 14.6 nm ($q^* = 0.50$ nm^{-1}), close to the TEM estimation.

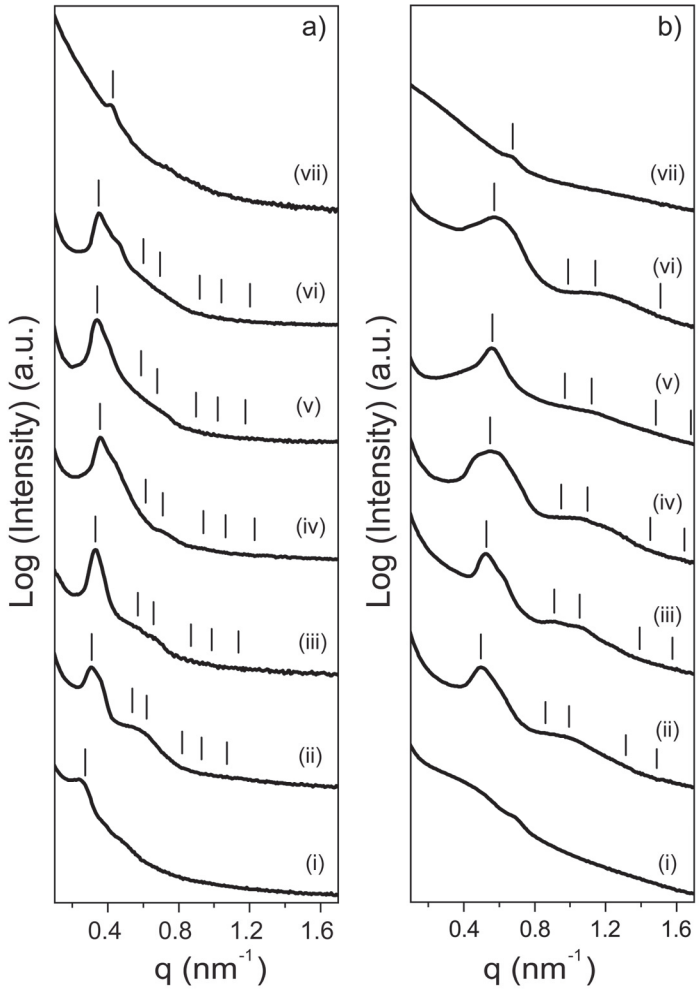

Figure 2. SAXS patterns of (a) F127–Al_2O_3 hybrids and (b) corresponding mesoporous Al_2O_3 samples after calcination at 450 °C in air, for (i) MA17-2, (ii) MA19-2, (iii) MA20-2, (iv) MA23-2, (v) MA26-2, (vi) MA28-2 and (vii) MA39-2, respectively. Tick marks indicate the principal peaks and expected higher-order reflections for *p6mm* symmetry.

Table 1. Structural analysis of F127–Al_2O_3 samples.

sample	q^* (nm^{-1})	*d*-spacing[a] (nm)	mesophase[a,b]
MA17-2	0.27	23.1	tubular / wormlike
MA19-2	0.31	23.4	*p6mm*
MA20-2	0.33	22.1	biphasic *p6mm* / $Im\bar{3}m$
MA23-2	0.36	20.5	biphasic *p6mm* / $Im\bar{3}m$
MA26-2	0.34	21.4	mixed *p6mm* / $Im\bar{3}m$ / wormlike
MA28-2	0.35	20.9	hierarchical, *p6mm*
MA28-2-DQ	0.34	21.6	hierarchical, *p6mm*
MA39-2	0.43	14.6	disordered
MA19-2-450	0.50	14.6	*p6mm*
MA20-2-450	0.53	13.8	biphasic *p6mm* / $Im\bar{3}m$
MA23-2-450	0.55	13.2	biphasic *p6mm* / $Im\bar{3}m$
MA26-2-450	0.56	12.9	mixed *p6mm* / $Im\bar{3}m$ / wormlike
MA28-2-450	0.57	12.7	hierarchical, *p6mm*
MA28-2-DQ-450	0.54	13.6	hierarchical, *p6mm*
MA23-1.8	0.39	18.5	*p6mm*
MA23-1.6	0.42	17.2	*p6mm*
MA23-1.4	0.46	15.6	*p6mm* / lamellar
MA23-1.2	0.46	13.8	*lamellar*
MA23-1.8-450	0.64	11.4	*p6mm*
MA23-1.6-450	0.68	10.7	*p6mm*
MA23-1.4-450	0.74	9.8	*p6mm* / lamellar
MA23-1.2-450	0.75	8.4	lamellar
MA23-1.6(BuOH)	0.45	16.1	*p6mm*
MA23-1.6(BuOH)-450	0.80	9.1	*p6mm*
MA23-2-700	0.62	11.8	biphasic *p6mm* / $Im\bar{3}m$
MA23-2-900	0.62 (*p6mm*) 0.50 ($Im\bar{3}m$)	11.8(*p6mm*) 17.9 ($Im\bar{3}m$)	biphasic *p6mm* / $Im\bar{3}m$
MA23-1.6-700	0.74	9.8	*p6mm*
MA23-1.6-800	0.72	10.1	*p6mm*
MA23-1.6-900	0.77	9.5	*p6mm*

[a] Determined by SAXS. [b] Determined by TEM and SEM of mesoporous Al_2O_3 samples.

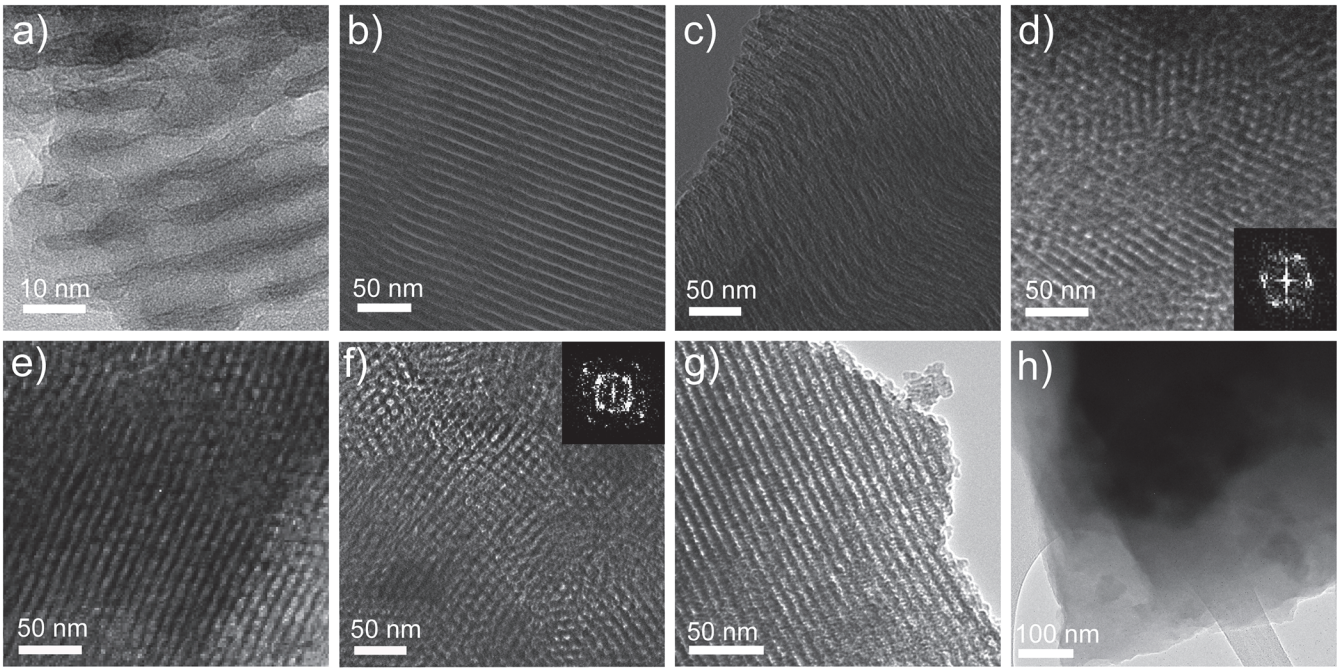

Figure 3. TEM micrographs (and FFT insets) of (a) tubular-type structure of MA17-2-450, (b) hexagonal cylinders of MA19-2-450, (c, d) biphasic MA20-2-450, (e, f) biphasic MA23-2-450, (g) hexagonal cylinders of MA26-2-450, and (h) lamellar structure of MA23-1.2-450. The (c) and (e) panels display the hexagonal cylinder morphology, while (d) and (f) panels display 3D cubic networks.

Interestingly, a new shoulder (q = 0.62 nm^{-1}) appears on the right side of the principal peak (q^* = 0.52 nm^{-1}) in the SAXS pattern of MA20-2-450 (sample (iii) in Figure 2b) after heat treatment, suggesting biphasic behavior (Figure S4). From TEM we observe both lying-down hexagonal cylinders in parallel (Figure 3c) and 3D cage-like cubic networks with four-fold symmetry (see Figure 3d and corresponding fast Fourier transform (FFT) inset). While it is difficult to assign a symmetry group with the current SAXS and TEM data, we postulate the cubic structure could belong to the $Im\bar{3}m$ family reported by Grant and coworkers (*vide infra*).[26] From TEM of the *p6mm* lattice in Figure 3c, we estimated the cylinder-to-cylinder *d*-spacing to be around 13.7 nm,

almost identical to the *d*-spacing of 13.8 nm from SAXS (sample (iii) in Figure 2b). And from TEM in Figure 3d, we measured a d_{100}-spacing (lattice parameter) of 13.1 nm and estimated the principal reflection of the $Im\bar{3}m$ morphology to be around $q^* = 0.68$ nm^{-1} (d_{110}-spacing = 9.2 nm), close to *q* value of the shoulder in the SAXS curve.

The broadening of principal peak is most prominent in the SAXS pattern of MA23-2-450 over the *q* range of 0.40–0.80 nm^{-1} (sample (iv) in Figure 2b), suggesting a strong presence of both *p6mm* and $Im\bar{3}m$ lattices, consistent with TEM characterization (Figure 3e, f and S5). In particular, the TEM image in Figure 3f presents both hexagonally arranged mesopores (top left corner) and four-fold 3D cubic networks. From TEM in Figure 3e, we estimated the cylinder-to-cylinder *d*-spacing of *p6mm* lattice is 11.3 nm relative to the SAXS value of 13.2 nm (sample (iv) in Figure 2b). The d_{110}-spacing and lattice parameter (d_{100}-spacing) of the $Im\bar{3}m$ lattice in Figure 3f are around 8.6 nm and 12.2 nm, respectively. We estimated the angular position of the $Im\bar{3}m$ principal reflection is around $q^* = 0.73$ nm^{-1}, i.e., within the broad range of the main SAXS peak. The slight difference in *d*-spacing values from TEM and SAXS analysis may be attributed to samples being tilted off their zone axes during TEM measurements.

The SAXS pattern for MA26-2-450 (sample (v) in Figure 2b) retains the principal peak but with diminished intensity and disappearance of higher order reflections, indicating some loss of long-range order. This is consistent with TEM and SEM observations where hexagonally arranged mesopore channels are observed (Figure 3g) together with regions of cubic (Figure S3c) and wormlike structures (Figure S3d), suggesting another stage of mesoporous Al_2O_3 structural evolution. From TEM (Figure 3g) the estimated cylinder-to-cylinder *d*-spacing of 9.2 nm is much smaller than the SAXS value (12.9 nm). We postulate this could be due to increased mesostructural inhomogeneities introduced by the disordered wormlike mesophase as well as

samples being tilted off their zone axes during TEM measurements. Further increase of Al_2O_3 composition led to spinodal decomposition-induced macro and mesophase separation for MA28-2-450 (sample (vi) in Figure 2b). SAXS (sample (vii) in Figure 2b) and TEM (Figure S3f) analysis indicate the highest Al_2O_3 composition of 39 wt% (MA39-2-450) resulted in a disordered structure.

The structural evolution of F127–Al_2O_3 mesophases can be explained by the critical packing parameter, $g = v/a_0 l$, where v is the volume of the hydrophobic block, a_0 is the effective area of hydrophilic components and l is the length of hydrophobic block.[42–44] Assuming the hydrophobic volume and length remain constant, the hydrolyzed Al_2O_3 sol additive is selectively attracted to the hydrophilic PEO block by hydrogen bonding, thereby increasing the a_0 and curvature of the hybrid F127–Al_2O_3 micelle but decreasing g.[24,38] The initial inorganic composition of 17 wt% Al_2O_3 was found to be inadequate to stabilize an ordered liquid crystal mesophase that eventually collapsed under heat treatment (MA17-2-450). Increasing the composition to 19 wt% Al_2O_3 (MA19-2-450) enabled formation of a thermally stable mesoporous Al_2O_3 with long-range *p6mm* order $(1/3 < g < 1/2)$. As the inorganic content reached 20 to 23 wt% Al_2O_3 (MA20-2-450 and MA23-2-450), the increase in the interfacial curvatures and higher effective hydrophilic contact area values (a_0) resulted in the decrease of packing parameters (g), initiating the shift to biphasic *p6mm* and $Im\bar{3}m$ $(g \leq 1/3)$ symmetries. For the higher composition of 26 wt% Al_2O_3, the mesostructure transited into the mixed *p6mm*, $Im\bar{3}m$ and wormlike structures (MA26-2-450). Most surprisingly, for the 28 wt% Al_2O_3 composition, the hybrid system crossed into the phase transformation of macroscale spinodal decomposition and mesoscale self-assembly.

Spinodal Decomposition Induced Formation of Hierarchically Ordered Al_2O_3. Hierarchical porous inorganic structures with well-ordered mesopores that facilitate mass flow and

accessibility at the macro and nanoscale levels as well as possessing high specific surface area, pore volume and structural stability, are highly desirable for many applications such as catalysis and separation. One approach to generate hierarchical porous Al_2O_3 structures is to have the homogenous organic-inorganic mixture enters a thermodynamically unstable state via chemical/physical stimuli such as composition and evaporation rate,[45,46] thereby crossing the phase boundary (spinodal line) to induce spinodal decomposition phase separation of two intermixed phases.[36,45,47–49] Tokudome and coworkers prepared mixtures of polyethylene oxide and propylene oxide to control gelation of Al_2O_3 salt precursors to induce spinodal decomposition phase separation of macroporous Al_2O_3 frameworks but without ordered mesoscale pores.[48] Wu and coworkers required adding trimethylbenzene as a swelling agent to increase the hydrophobic core of P123–Al_2O_3 micelle resulting in disordered porous Al_2O_3 structures with pore size distribution of 6–600 nm.[36] Here we found that by simply adding ~28 wt% of Al_2O_3 additive into the F127 solution and upon ethanol evaporation, spinodal decomposition occurred spontaneously resulting in F127-rich phase and ordered F127–Al_2O_3-rich phase. Thermal annealing in air removed the BCP to form hierarchical ordered Al_2O_3 structures comprising interconnected networks of macroscale pores and well-ordered mesoporous channels with *p6mm* symmetry as shown in Figure 4.

Figure 4a shows a freshly fractured cross-section of the MA28-2-450 monolith with randomly distributed macroscale pores of 1–5 μm (Figure 4b, c). SEM (Figure 4d) and TEM (Figure 4e) images of higher magnifications show the inorganic Al_2O_3 struts consist of parallelly aligned mesopore channels with the distinctive honeycomb symmetry (*p6mm*). SAXS data corroborate the majority of MA28-2-450 mesostructure has the *p6mm* symmetry (sample (vi) in Figure 2b) with a cylinder-to-cylinder *d*-spacing of 12.6 nm. We also found some regions of wormlike

structure in TEM (Figure S3e) that could explain for the shoulder feature next to the principal peak in the hybrid SAXS curve (sample (vi) in Figure 2a). To the best our knowledge, this is the first report of spinodal decomposition-induced hierarchical porous Al_2O_3 monolith with periodic hexagonal mesopore channels.

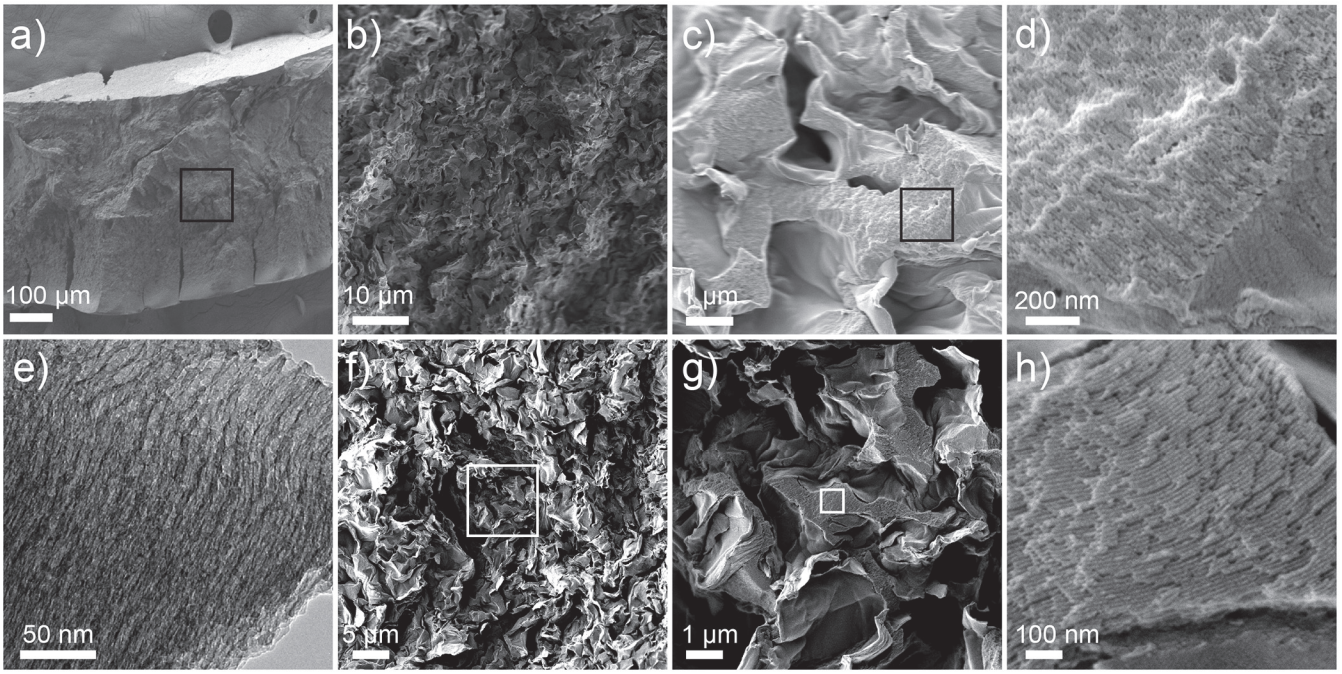

Figure 4. (a–d) SEM and (e) TEM micrographs of hierarchical MA28-2-450. The highlighted regions denoted in (a) and (c) are shown at higher magnifications in (b) and (d), respectively. (f–h) SEM images of hierarchical MA28-2-DQ-450 obtained at faster solvent evaporation rate, resulting in a deeper quench depth. The highlighted regions denoted in (f) and (g) are shown at higher magnifications in (g) and (h), respectively.

The synthesis of spinodal decomposition induced hierarchical ordered Al_2O_3 is robust and highly reproducible. For instance, we fabricated ten other hybrid MA28-2 samples and found eight of them having highly similar morphology as confirmed by SAXS (Figure S6a, b). The samples were then thermally annealed in air at 450 °C and 700 °C for nitrogen sorption analysis. The

nitrogen isotherm of hierarchical MA28-2-450 exhibits a Type IV H1 hysteresis (Figure S7a) with a sharp capillary condensation step at ~0.7P/P_0, indicating uniform pore size and good connectivity. The BET surface area and BJH pore size are 63 m^2/g and 6.9 nm (Figure S7b), respectively, with micropores contributing about 16% of the specific surface area (Table 2). Even after heating at the higher 700 °C, the hierarchical ordered Al_2O_3 remained stable retaining the *p6mm* lattice as confirmed by SAXS (Figure S6c). The nitrogen isotherm of MA28-2-700 exhibits a hysteresis loop that is closer to Type IV H2 (Figure S7a). While the BJH pore size was reduced by ~10% to 6.2 nm (Figure S7b), the specific area increased by ~20% to 76 m^2/g with negligible micropore contribution. We speculate at 700 °C, the hierarchical Al_2O_3 structures densified closing the micropores and crystallized into γ-Al_2O_3 at the surface (Figure S9a).[15] The newly formed small crystallites may have protruded slightly out of the mostly amorphous wall surface, increasing the total surface area but retained mesoscale structural stability.

We found that the macropore structure can be tuned by controlling the evaporation rate. SEM images of MA28-2-DQ-450 in Figure 4f–h show a new form of hierarchically ordered porous Al_2O_3 structures generated by increasing the evaporation rate, thereby inducing a deeper quench depth in the spinodal decomposition region.[45,46] Figure 4f and g reveal a macroscopic pore structure with higher degrees of openness whilst maintaining the highly ordered hexagonally aligned cylindrical mesopores (Figure 4h). This is corroborated by the SAXS spectra exhibiting multiple reflections with strong intensities for both hybrid and 450 °C-annealed Al_2O_3 samples (Figure S8a). From nitrogen sorption analysis (Figure S8b, c), MA28-2-700-DQ exhibits a Type IV isotherm with H1 hysteresis attributed to uniform cylindrical pores and a larger surface area of 194 m^2/g that is comparable with the quasi-equilibrium mesoporous Al_2O_3 (i.e., 160–210 m^2/g). This suggests the deeper-quenched hierarchical MA28-2-DQ sample consists of highly

accessible co-continuous macropore networks interconnected with ordered hexagonal mesopore channels, while MA28-2 contains more isolated macroscale domains resulting in lower surface area.[46]

Table 2. Textural characteristics of mesoporous Al_2O_3.

sample	pore size,[a] nm	BET surface area, m^2/g (micropore area,[b] m^2/g)	pore volume,[c] cm^3/g (micropore volume, cm^3/g)[c]	crystallite size,[d] nm	CO_2 sorption @ 0 °C, mmol/g	CO_2 sorption @ 25 °C, mmol/g
MA23-2-450	7.0	149 (18)	0.29 (0.007)		0.66	
MA23-2-700	6.3	158 (3)	0.25 (0.0002)	<1	0.61	
MA23-2-900	5.8	118 (11)	0.20 (0.004)	5-6	0.65	
MA28-2-450	6.9	63 (10)	0.12 (0.004)		0.37	
MA28-2-700	6.2	76	0.10		0.46	
MA28-2-DQ-700	7.5	194 (25)	0.33 (0.01)		0.87	0.54
MA23-1.6-450	6.2	185 (17)	0.32 (0.006)			
MA23-1.6-700	6.0	207 (23)	0.31 (0.008)	1–2		
MA23-1.6-800				3-4		
MA23-1.6-900	5.0	159 (7)	0.21 (0.002)	4-5		
MA23-1.6(BuOH)-450	2.5, 5.3, 11.9	305 (67)	0.33 (0.026)		1.69	1.14
Commercial-Al_2O_3	6.1	123	0.26		0.43	0.23

[a] Determined by BJH and KJS models from nitrogen sorption analysis. [b] Determined by *t*-plot method from nitrogen sorption analysis. [c] Single point pore volume at 0.99 P/P_0. [d] Determined from PXRD.

Influence of HNO_3/Al Ratios on Ordered Al_2O_3 Mesophases. In previous studies of Pluronic BCP–Al_2O_3 mesostructures, Yuan *et al*. reported the most stable hexagonal *p6mm* morphology were formed at HNO_3/Al molar ratios of 2.0–2.4,[6] while Grant *et al*. observed phase transitions of *p6mm* to cage-like cubic lattices at higher HNO_3/Al ratios of 3.0–4.0.[27] In our present study, colorless transparent Al(O^sBu)$_3$–derived sol nanoclusters were prepared in separate reaction vessels for different durations (12–60 h) before mixing with F127 BCP, enabling precise control to investigate alternative ordered F127–directed Al_2O_3 morphologies at relatively unexplored lower acid/metal ratios.

Figure 5a shows the SAXS patterns of various F127–directed Al_2O_3 hybrids with the same inorganic composition (23 wt% Al_2O_3) but synthesized under different HNO_3/Al molar ratios of 1.2–1.8. Compared to MA23-2 hybrid sample (Figure 2a), the intensity and width of the principal SAXS peak of MA23-1.8 hybrid (sample (i) of Figure 5a) become higher and narrower, respectively, indicating improved *p6mm* symmetry as HNO_3/Al ratio reduced from 2 to 1.8. The most significant structural enhancement is observed in the SAXS pattern of MA23-1.6 hybrid (sample (ii) of Figure 5a) with the highest principal peak intensity and appearance of new higher order reflections at $(q/q^*)^2 = 4$ and 7, i.e., MA23-1.6 has the most well-defined hexagonal *p6mm* lattice with long-range order. As a demonstration we conducted scale-up EISA experiments of MA23-1.6 hybrids in larger crystallization dishes of 5-cm and 7.5-cm-diameters (compared to PTFE beaker of 2.1-cm-diameter) and consistently obtained long-range ordered hexagonal morphology (see SAXS data in Figure S10a). For HNO_3/Al ratio of 1.4, while the SAXS pattern remains consistent with *p6mm*, the decrease of intensity of the principal peak and shift to higher q value, along with the disappearance of secondary reflections, suggest an impending mesophase transition (sample (iii) of Figure 5a). Finally, for HNO_3/Al of 1.2, the intensities of SAXS reflections improve substantially at new angular positions of $(q/q^*)^2 = 1, 4$, consistent with the lamellar lattice (sample (iv) of Figure 5a).

SAXS data in Figure 5b (samples (i)–(iii)) and S10 show that mesoporous Al_2O_3 samples of HNO_3/Al ratios of 1.8, 1.6 and 1.4, retained the principal and secondary reflections of long-range *p6mm* order after thermal annealing at 450 °C and 700 °C in air, and corroborated by TEM (Figure S3g–i). We further observe layered structures in the TEM of MA23-1.4-450 (Figure S3j), suggesting biphasic hexagonal and lamellar characteristics attributed to mesophase transition. Conversely the SAXS peaks of MA23-1.2-450 disappear almost completely after BCP removal

(sample (iv) of Figure 5b), indicating collapse of lamellar mesophase into sheet-like structures (see TEM in Figure 3h and S3k). To the best of our knowledge, this is first report of 2D lamellar lattice in a Pluronic BCP-directed Al_2O_3 monolith.

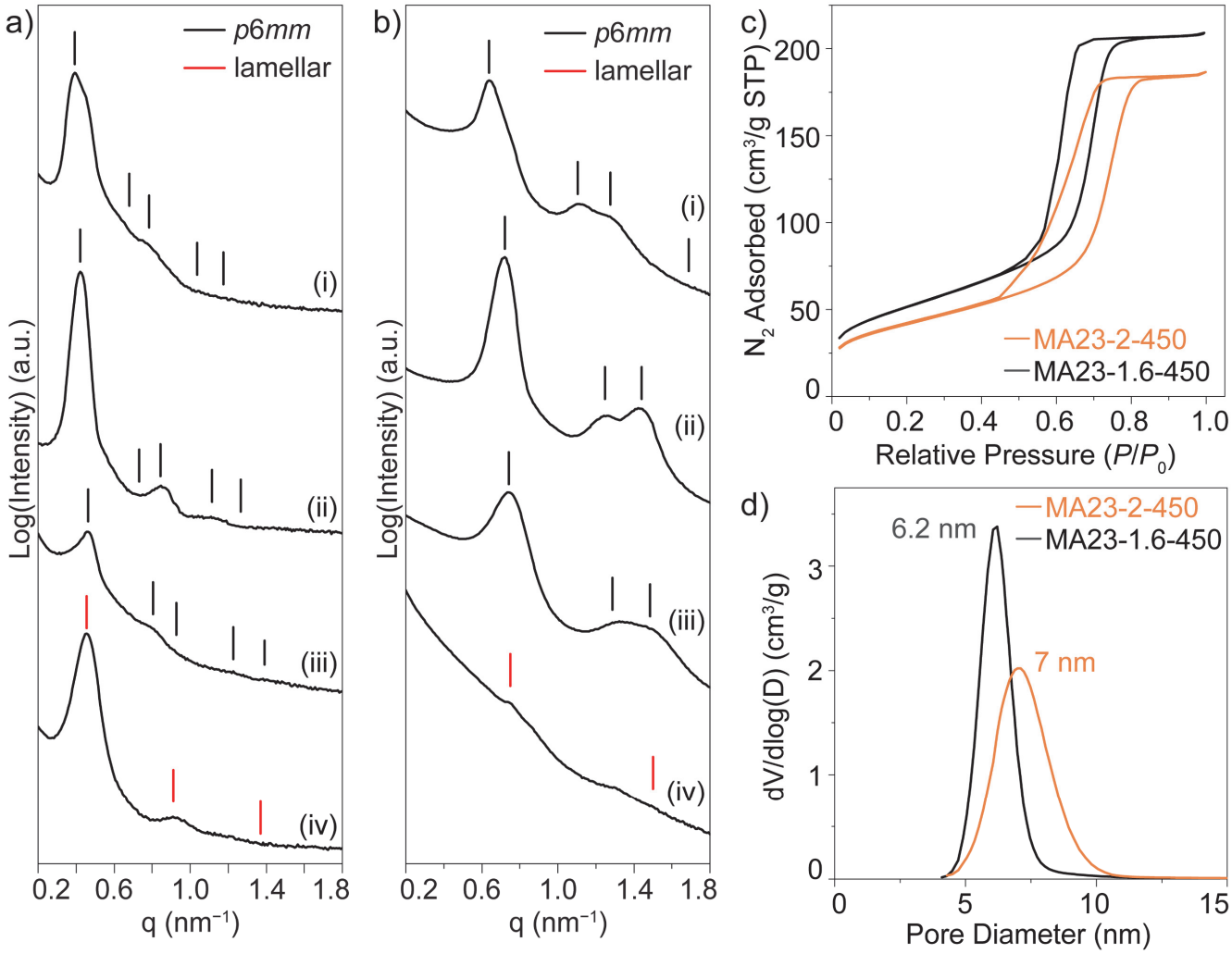

Figure 5. (a,b) SAXS patterns of (a) MA-23 hybrids and (b) corresponding mesoporous Al_2O_3 samples annealed at 450 °C for HNO_3/Al acid molar ratios of (i) 1.8, (ii) 1.6, (iii) 1.4 and (iv) 1.2. Tick marks indicate expected SAXS reflections for *p6mm* (black) and lamellar (red) lattices. (c) Nitrogen sorption isotherms and (d) pore size distributions of MA23-2-450 and MA23-1.6-450 samples.

This order-to-order mesophase transition is congruous with the simultaneous increase of critical packing parameter (g) and decrease of F127–Al_2O_3 micelle curvature as HNO_3/Al molar ratios reduced from 2 to 1.2. HNO_3 is the catalyst and H_2O source for hydrolysis of $Al(O^sBu)_3$. With less added HNO_3 the kinetics of hydrolysis of Al_2O_3 sol nanoclusters slowed down significantly requiring longer durations (from 6 to 60 h) to form the colorless transparent inorganic additive in EtOH. Upon mixing the Al_2O_3 sol precursors with F127 BCP solution, it is likely that the hybrid micelle diameter decrease in size with less amounts of H^+, NO_3^- and H_2O swelling the PEO-corona,[50] resulting in lower effective hydrophilic contact area values (a_0) and interfacial curvatures, but higher packing parameters (g). This is consistent with the decreasing *p6mm d*-spacing values from 21.4 to 15.6 nm (~27%) as the HNO_3/Al ratio changed from 2 to 1.4. For the HNO_3/Al ratio of 1.2, the even smaller micelle interfacial curvature induced a phase transition from *p6mm* to lamellar lattice of zero mean curvature ($g \approx 1$).

Nitrogen sorption measurements provided further structural and textural properties of mesoporous MA23-2-450 and MA23-1.6-450 samples. Figure 5c shows MA23-2-450 exhibits a sorption isotherm of Type IV H1 hysteresis loop with delayed desorption, suggesting mesoporous samples with cage-like pores.[27] This is consistent with our earlier observations of mixed cubic and hexagonal morphologies in SAXS (Figure 2b) and TEM (Figure 3e, f). In contrast, the sharp and vertical capillary step in the sorption isotherm indicates MA23-1.6-450 has a Type IV with H1 hysteresis loop (Figure 5c), representing highly uniform cylindrical pores and improved pore size distribution (Figure 5d). Furthermore, as the HNO_3/Al ratio reduced from 2 to 1.6, there was a decrease of pore size from 7 nm to 6.2 nm (Figure 5d) likely due to less H^+, NO_3^- and H_2O species interacting with the smaller hybrid micelles, and increase of surface area and pore volume by 24% and 10% (Table 2), respectively.

We further postulate lower HNO_3/Al ratios promote formation of smaller sized Al_2O_3 sol nanoclusters over longer reaction durations.[51] Smaller Al_2O_3 nanoclusters interacting with the PEO-based corona may enable favorable translation entropic gains and advocate growth of well-defined homogeneous mesophases (e.g., compare MA23-2 and MA23-1.6 samples).[51,52] Finally, we summarized the collected data of F127–Al_2O_3 hybrid monoliths in a morphology map as a function of F127/Al_2O_3 composition and HNO_3/Al molar ratio (Figure 6).

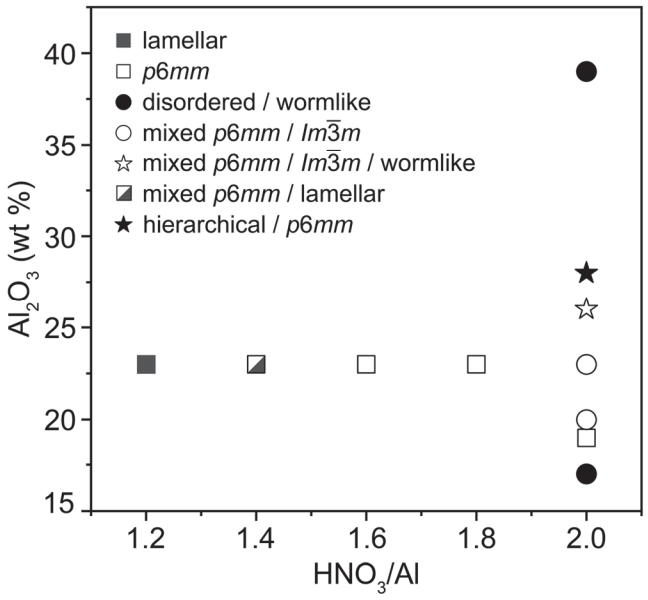

Figure 6. Morphology map of F127–Al_2O_3 hybrid monolith samples by EISA as a function of F127/Al_2O_3 composition and HNO_3/Al molar ratio.

Influence of Solvent on Porosity of Ordered Mesoporous Al_2O_3. It is well-established that the solubilizing medium greatly affects the sol–gel reaction kinetics of Al alkoxides as well as resultant block copolymer–directed mesophases.[4,35,53] To investigate the solvent influence, Al(O^sBu)$_3$ was added into the less polar *n*-BuOH in place of EtOH. This results in the exchange of *sec*-butoxyl ligands with linear *n*-butoxyl ligands surrounding the Al^{3+} ions.[15,35,53] Adding HNO_3 catalyzed the hydrolysis and condensation reactions (HNO_3/Al = 1.6). The transparent *n*-

BuOH based Al_2O_3 sol additive was then added into a solution of F127 in EtOH (23 wt% Al_2O_3), followed by EISA to form a hybrid monolith denoted as MA23-1.6(BuOH).

Figure S11a shows the SAXS patterns of the as-made hybrid MA23-1.6(BuOH) and mesoporous Al_2O_3 after thermal annealing at 450 °C (MA23-1.6(BuOH)-450). Compared to EtOH-derived MA23-1.6 (sample (ii) in Figure 5a), the principal SAXS peak of hybrid MA23-1.6(BuOH) has a lower intensity and even weaker secondary peaks at higher q values, suggesting a lower degree of *p6mm* order (black curve in Figure S11a). But after thermal annealing at 450 °C, SAXS data shows the hexagonal *p6mm* order improved as indicated by the presence of the principal and higher order reflections (MA23-1.6(BuOH)-450, gray curve in Figure S11a). Figure S11b shows the nitrogen sorption isotherm of MA23-1.6(BuOH)-450 that is classified as Type IV with H2 hysteresis. The three capillary condensation steps observed at P/P_0 of 0.6, 0.75 and 0.95, suggest presence of mesopores with different pore sizes. BJH analysis revealed a trimodal mesopore size distribution of 2.5, 5.3 and 11.9 nm (Figure S11c). Micropores (<2 nm) further contributed about 22% and 8% to the total BET surface area and pore volume of 305 m^2/g and 0.33 cm^3/g, respectively.

Using *n*-BuOH as solvent further slowed the hydrolysis and condensation reactions of $Al(O^sBu)_3$ compared in the EtOH environment.[35] The longer *n*-butoxy ligands likely introduce steric effects that inhibit hydroxyl groups from approaching Al^{3+} cations and form Al_2O_3 sol nanoclusters with varying degrees of polymerization.[35] This may cause weaker interactions between the inorganic sol nanoclusters and F127 PEO blocks, disrupting mesophase ordering into better defined *p6mm* lattice.[37] The increase of microporosity could arise from poorly coordinated random packing of Al_2O_3 sol species at the mesostructure interfaces. We also cannot exclude the less polar *n*-BuOH (dielectric constant of 17.7 compared to the dielectric constant of EtOH of 25) may have lesser

ability to solvate and stabilize the protonated Al_2O_3 intermediates to form homogenous mesophases with the soft BCP template.[53,54]

Thermal Annealing of Mesoporous Al_2O_3. Mesoporous Al_2O_3 samples were thermally annealed from 450 °C to 1000 °C in air and characterized by SAXS, PXRD, TEM and nitrogen sorption to determine their structural and textural properties and thermal stability. SAXS (Figure 7a) and TEM (Figure 7c, d and S12) show that mesoporous MA23-2 samples retained biphasic hexagonal *p6mm* and cubic $Im\bar{3}m$ morphologies with various degrees of long-range order for 700 and 900 °C. More interestingly, we observe large grain areas of MA23-2-900 exhibiting highly intense SAXS reflections at angular positions of $(q/q^*)^2 = 1, 2, 3$, consistent with the $Im\bar{3}m$ lattice (Figure 7a).[24] HR-TEM images in Figure 7d and S12 corroborate the highly crystalline Al_2O_3 *p6mm* and network-like structures for MA23-2-900, respectively. Similarly, SAXS confirmed the preservation of long-range *p6mm* symmetry for mesoporous MA23-1.6-900 samples (Figure S9b). Remarkably, optical images and SAXS data in Figure S9 show the MA23-1.6-900 samples retained both macroscale free-standing monolithic shape and mesoscale *p6mm* symmetry after annealing at 900 °C, with very similar thermal-induced shrinkage of 45% and 48% in the millimeter (optical) and nanometer (SAXS) length scales, respectively, validating high thermal and structural integrity.

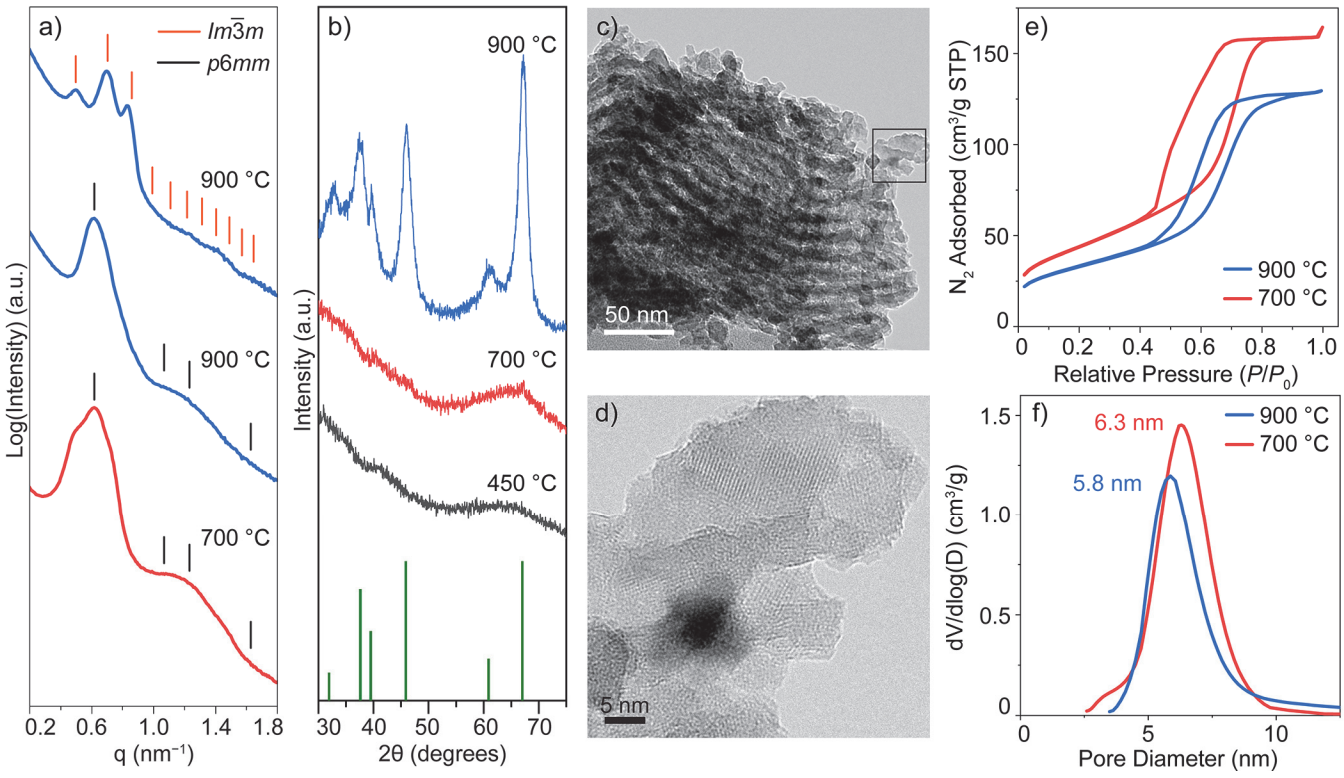

Figure 7. (a) SAXS and (b) PXRD patterns of mesoporous MA23-2 samples after thermal annealing at 450 °C (gray), 700 °C (red) and 900 °C (blue) in air. Tick marks in (a) indicate the expected SAXS reflections of *p6mm* (black) and *Im*$\bar{3}$*m* (orange) lattices. PXRD peak markings and relative intensities for γ-Al_2O_3 (green, PDF 00-010-0425) are shown in (b). (c, d) TEM of hexagonal cylinders of MA23-2-900. The highlighted region in (c) is shown under higher magnification by HR-TEM in (d). (e) Nitrogen sorption isotherms and (f) pore size distributions of mesoporous MA23-2-700 and MA23-2-900.

PXRD patterns of mesoporous MA23-2 and MA23-1.6 samples in Figure 7b and Figure S9a, respectively, illustrate the crystalline phase transformation of Al_2O_3 after thermal annealing in air. All mesoporous Al_2O_3 were amorphous after annealing at 450 °C. While the inorganic mesostructure remained primarily amorphous at 700 °C, the appearance of a broad peak at 2θ = 67° indicates formation of small crystallites oriented to the (440) plane of γ-Al_2O_3 (PDF 00-010-

0425). Nucleation and growth of new crystallites in the ordered mesoporous Al_2O_3 structures occurred at 800 °C and 900 °C, denoted by emergence of new PXRD reflections with higher intensities and narrower widths as well as observations of crystalline fringes from HR-TEM (Figure 7d and S12b). From the Scherrer equation, we estimated the γ-Al_2O_3 crystallite size grew to around 4 and 6 nm at 800 °C and 900 °C, respectively. From SAXS and PXRD, the mesoporous structure transformed into crystalline θ- and α-Al_2O_3, thereby collapsed at 1000 °C (Figure S9).[55]

Nitrogen sorption analysis of MA23-2-700 and MA23-2-900 exhibit Type IV isotherms and hysteresis loops with mixed H1 and H2 characteristics, consistent with the biphasic hexagonal *p6mm* and cage-like $Im\bar{3}m$ morphologies of the mesoporous samples (Figure 7e). Whereas MA23-1.6-700 and MA23-1.6-900 display Type IV isotherms with H1 hysteresis, confirming presence of highly ordered hexagonal mesopore channels (Figure S13a). BJH pore size of mesoporous MA23-2 and MA23-1.6 samples decreased from 7.0 to 5.8 nm and 6.2 to 5.0 nm, respectively, after thermal annealing from 450 to 900 °C due to crystallization (Figure 5d, 7f and S13b). What is surprisingly is that the highest BET surface areas of MA23-2 and MA23-1.6 samples (i.e., 158 and 207 m^2/g, respectively) were obtained after annealing at 700 °C, similar to the hierarchical ordered MA28-2-700 samples (*vide supra*). This is likely due to the formation of small γ-Al_2O_3 crystallites at the surface increasing the overall available surface area for nitrogen adsorption.[15] The BET surface areas of MA23-2-900 and MA23-1.6-900 then decreased by ~25% to 118 m^2/g and 159 m^2/g, respectively, upon further γ-Al_2O_3 crystallization at 900 °C (Figure 5e and S13).

Adsorption Characteristics for Carbon Dioxide and Congo Red Dye. With high surface area and thermal/chemical stability, mesoporous Al_2O_3 are promising solid adsorbents for

environmental applications such as carbon dioxide (CO_2) capture and wastewater filtration.[2,7,9,10] We first evaluated the (physical) adsorption properties of ordered mesoporous Al_2O_3 for CO_2 at 0 °C and 25 °C for 1 bar displayed in Figure 8a and S11d, as well as summarized in Table 2. MA23-1.6(BuOH)-450 has the highest CO_2 adsorption capacity of 1.69 and 1.14 mmol/g at 0 °C and 25 °C for 1 bar, respectively, attributed to the high surface area, pore volume and microporosity.[56,57] However, even as mesoporous MA23-2 samples have varying BET surface areas after annealing at 450–900 °C (149–118 m^2/g), they share very similar CO_2 adsorption capacities of 0.61–0.66 mmol/g at 0 °C likely due to lower microporosity and constrained pore access for CO_2 adsorption caused by the mixed hexagonal and cubic morphologies. Nonetheless, ordered mesoporous MA23-2 and MA23-1.6(BuOH) samples have higher CO_2 adsorption capacities than commercial-Al_2O_3 (Figure S14a).

The hierarchical MA28-2-450 has the lowest BET surface area and CO_2 adsorption capacity of 63 m^2/g and 0.37 mmol/g (0 °C), respectively. Intriguingly, after annealing at 700 °C both BET surface area and CO_2 adsorption capacity of MA28-2-700 increased by more than 20% to 76 m^2/g and 0.46 mmol/g (0 °C), respectively. Unlike MA23-1.6(BuOH)-450, nitrogen sorption analysis indicates negligible micropores in MA23-2-700. We postulate the higher-than-expected CO_2 loading capacity could arise from enhanced CO_2 flow transport efficiency and surface accessibility imparted by the hierarchically interconnected pore networks of macropores and hexagonally ordered mesopores (Figure 4). By increasing the solvent evaporation rate to reach a deeper quench state in the spinodal decomposition region, the interconnectivity and accessibility of the macropore domains drastically improved for hierarchical MA23-2-DQ-700, thereby increasing the BET surface area and CO_2 adsorption capacity to 196 m^2/g and 0.87 mmol/g (0 °C), respectively (Figure S8b, d). At 25 °C, the CO_2 adsorption capacity of MA23-2-DQ-700

(0.54 mmol/g) is more than doubled of commercial-Al_2O_3 (0.23 mmol/g). Moreover, our CO_2 adsorption capacity values (i.e., 0.5–1.69 mmol/g) are comparable to other mesoporous Al_2O_3 systems (0.5–1.36 mmol/g).[7,8]

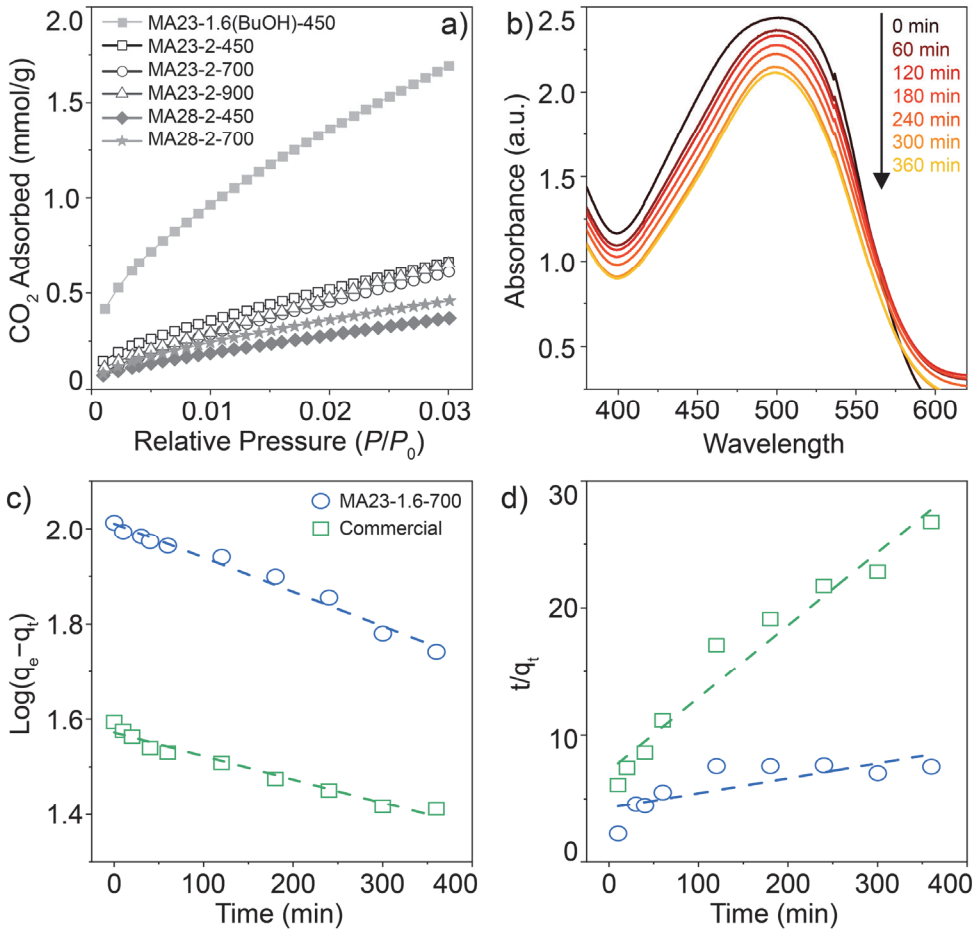

Figure 8. (a) CO_2 adsorption isotherms of ordered mesoporous Al_2O_3 samples measured at 0 °C for 1 bar. (b) Absorbance spectra of Congo red aqueous solution after treatment with MA23-1.6-700 at different time points as indicated. (c) Pseudo-first and (d) pseudo-second order kinetics of Congo red dye adsorption by MA23-2-700 (blue circle) and commercial Al_2O_3 (green square). The dotted lines in (c) and (d) were obtained from linear regression analysis using the respective data points.

The 2–50 nm pore size of mesoporous solid adsorbents permits CO_2 capture under both low- and high-pressure conditions.[57,58] Xu *et al*. reported an impressive loading of 5.39 mmol/g of CO_2 (75 °C, 1 bar) using amine-functionalized mesoporous SBA-15 silica structures.[59] However, amorphous silica exhibits low hydrothermal stability with extremely slow CO_2 adsorption kinetics.[57,58,60] Estevez et al. investigated the CO_2 adsorption capacity of hierarchical porous carbon by varying the trimodal pore sizes (<2-nm, 7 and 40-nm, 1–20-μm), surface areas (1500–2800 m^2/g) and pore volumes (1–10 cm^3/g), obtaining the CO_2 loading of 3.7 mmol/g (25 °C for 1 bar).[61] However, the multistep synthesis protocol is highly complex and energy intensive, such as employing different hard templates (ice templating and silica colloids), long pyrolysis durations at high temperatures, as well as template removal and carbon activation.[61] We postulate a facile one-pot synthesis approach to form hierarchically ordered mesoporous Al_2O_3 structures with excellent mass transport and accessibility characteristics could enable more selective and higher CO_2 adsorption capabilities via surface functionalization with amine groups and/or incorporation with alkaline metal components.[2,7]

Next, we investigated the adsorption properties of hexagonally ordered MA23-1.6-700 and commercial-Al_2O_3 for Congo red dye as a model wastewater pollutant. To obtain the equilibrium adsorption capacities, 10 mg of finely powdered mesoporous Al_2O_3 was immersed in a 70 mL of Congo red solution with an initial concentration (C_0) of 50 mg/L for 24 h. It should be mentioned that a significant excess amount of Congo red was used in our experiments to probe the kinetics of dye adsorption in mesoporous Al_2O_3 (i.e., 3.5 mg of dye per 10 mg of Al_2O_3 compared to 1.125 mg of dye per 10 mg of Al_2O_3 in ref. 9). An aliquot was then retrieved from each sample to determine the equilibrium dye concentration (C_e) from absorbance measurement at 498 nm. The equilibrium adsorption capacities summarized in Table 3 were calculated using the equation

$q_e = (C_0 - C_e)v/m$, where v is the volume of dye solution and m is the mass of mesoporous Al_2O_3.

Table 3: Summary of Congo red dye adsorption kinetics.

sample	q_e,[a] mg/g	pseudo-first order model			pseudo-second order model		
		k_1,[b] g/mg min	theoretical q_e,[c] mg/g	R^2	k_2,[d] g/mg min	theoretical q_e,[c] mg/g	R^2
MA23-1.6-700	103.05	2.1×10^{-3}	102.52	0.9824	3.27×10^{-5}	84.75	0.6034
Commercial-Al_2O_3	39.27	1.2×10^{-3}	37.33	0.9654	4.5×10^{-4}	17.51	0.9549

[a] Experimental equilibrium Congo red dye adsorption capacity. [b] Pseudo-first order kinetic constant derived from linear regression. [c] Theoretical equilibrium adsorption capacity derived from linear regression. [d] Pseudo-second order kinetic constant derived from linear regression.

The most promising Al_2O_3 adsorbent for Congo red is MA23-1.6-700 with an equilibrium adsorption capacity of 103 mg/g, whereas commercial-Al_2O_3 only adsorbed around 40 mg/g of dye molecules after 24 h. We postulate that the commercial-Al_2O_3 may have fewer available adsorption sites due to lower BET surface area and pore volume compared to MA23-1.6-700 (123 m^2/g and 0.26 cm^3/g versus 207 m^2/g and 0.31 cm^3/g, respectively) despite having similar pore diameters (~6 nm) (Figure S14c, d). Another possible reason is better pore accessibility inherited from the highly ordered hexagonal symmetry (Figure S10b). This is consistent with the faster dye removal rate by MA23-1.6-700 inferred from the absorbance spectra of Congo red solution collected at hourly intervals in Figure 8b. The amount of dye removed was the highest within the first 60 min (see black and dark brown curves), followed by a slight slow-down in the next 60 min (see dark brown and red curves for 60 and 120 min time points), and then drastically increased over the next 3 h (see the red to orange curves for 120 to 300 min time points). This indicates a strong affinity of the dye molecules to the well-ordered and accessible Al_2O_3 mesopore channel walls. In contrast, dye adsorption by commercial-Al_2O_3 reached steady state after the first 60 min (Figure S14e).

To further quantify dye adsorption behaviors by mesoporous Al_2O_3, we applied the pseudo-first and pseudo-second order kinetic models[62] using Equation (1) and (2), respectively,

$$\log(q_e - q_t) = \log q_e - \frac{k_1 t}{2.303} \quad (1)$$

$$\frac{t}{q_t} = \frac{1}{k_2 q_e^2} + \frac{t}{q_e} \quad (2)$$

where q_e and q_t (mg/g) are the Congo Red adsorption capacities at equilibrium and time point t (min), and k_1 (g/mg min) and k_2 (g/mg min) are the pseudo-first and pseudo-second order rate constants derived from linear regression. The time dependent adsorption capacity was calculated from $q_t = (C_0 - C_t)v/m$, where C_t is the dye concentration at time point t obtained from absorbance measurement. The linear regression plots and calculated kinetic parameters of mesoporous MA23-1.6-700 and commercial-Al_2O_3 are presented in Figure 8 and Table 3. From linear regression analysis, the pseudo-first order kinetic model is more appropriate to describe Congo red dye adsorption behaviors for both mesoporous Al_2O_3 samples (Figure 8c). Moreover, the calculated adsorption capacities at equilibrium (theoretical q_e) are almost identical to the measured values (q_e). Consistent with our absorbance spectra interpretation, the pseudo-first order kinetic constant (k_1) for Congo red adsorption of MA23-1.6-700 is higher than commercial-Al_2O_3 by a factor of almost 2.

CONCLUSIONS

We demonstrated an EISA-based approach to generate a myriad of long-range and well-defined F127–Al_2O_3 hybrid mesophases. Decoupling the $Al(O^sBu)_3$ sol-gel reaction before mixing with the BCP, enabled access to a wider and relatively unexplored parameter space of F127/Al_2O_3 composition and HNO_3/Al molar ratio, forming 2D lamellar, hexagonal *p6mm* and 3D cubic

Im$\bar{3}$*m* lattices. The formation pathways of order-to-order mesophase transitions were elucidated from the interactions of Al_2O_3 sol nanoclusters, H_2O, H^+ and NO_3^- ions with F127 PEO blocks, inducing changes in the micelle curvature and critical packing factor. Exchanging the solvent from EtOH to *n*-BuOH provided further leverage slowing the sol–gel hydrolysis and condensation reactions of $Al(O^sBu)_3$ to yield hexagonally arranged mesoporous Al_2O_3 with surface area and pore volume of 305 m^2/g and 0.33 m^3/g, respectively. Further increase in Al_2O_3 composition and faster solvent evaporation rate induced spinodal decomposition in the BCP-additive blend to form F127-rich phase and well-ordered F127–Al_2O_3-rich phase. Thermal annealing in air up to 900 °C removed the copolymer and yielded long-range ordered mesoporous γ-Al_2O_3 structures as well as hierarchically porous γ-Al_2O_3 structures with interconnected networks of macropores and well-ordered mesopore channels with *p*6*mm* symmetry. The resultant ordered mesoporous Al_2O_3 exhibited high affinities to capture CO_2 and Congo red dye for potential high temperature adsorption and wastewater filtration applications. Our results summarized as a two-component morphology map may serve as a guide for future structure–property studies and synthesis of alternative Al_2O_3-based oxides and advanced ceramics with well-ordered morphologies for urban sustainability and clean energy-related applications.

ASSOCIATED CONTENT

Supporting Information

The Supporting Information is available free of charge at https://pubs.acs.org/doi/10.1021/

Additional characterization of F127–Al_2O_3 hybrids and mesoporous Al_2O_3 samples by SAXS, PXRD, SEM, TEM, TGA, nitrogen/carbon dioxide sorption analysis and UV-vis spectroscopy.

AUTHOR INFORMATION

Corresponding Author

Kwan W. Tan – E-mail: kwtan@ntu.edu.sg

Complete contact information is available at: https://pubs.acs.org/10.1021/

Author Contributions

G.L.S. and L.W. contributed equally to the work.

Notes

The authors have no competing financial interest.

ACKNOWLEDGMENT

This work was supported by a member-directed research grant from ExxonMobil through the Singapore Energy Center (EM11161.TO6) and a startup grant from Nanyang Technological University, Singapore. This work made use of research facilities at the Facility for Analysis, Characterization, Testing and Simulation (FACTS), Nanyang Technological University, Singapore. C.T. gratefully acknowledges an overseas training program grant from King

Mongkut's Institute of Technology Ladkrabang. The authors thank H. Sai, J. G. Werner, S. K. Yeow, D. Calabro, E. Corcoran and S. Weston for helpful discussions.

REFERENCES

(1) Seki, T.; Onaka, M. Mesoporous Alumina: Synthesis, Characterization, and Catalysis. In *Advanced Nanomaterials*; Geckeler, K. E., Nishide, H., Eds.; Wiley-VCH Verlag GmbH & Co. KGaA, 2009; pp 481–521.

(2) D'Alessandro, D. M.; Smit, B.; Long, J. R. Carbon Dioxide Capture: Prospects for New Materials. *Angew. Chem., Int. Ed.* **2010**, *49*, 6058–6082.

(3) Xu, X.; Megarajan, S. K.; Zhang, Y.; Jiang, H. Ordered Mesoporous Alumina and Their Composites Based on Evaporation Induced Self-Assembly for Adsorption and Catalysis. *Chem. Mater.* **2020**, *32*, 3–26.

(4) Vaudry, F.; Khodabandeh, S.; Davis, M. E. Synthesis of Pure Alumina Mesoporous Materials. *Chem. Mater.* **1996**, *8*, 1451–1464.

(5) Niesz, K.; Yang, P.; Somorjai, G. A. Sol-Gel Synthesis of Ordered Mesoporous Alumina. *Chem. Commun.* **2005**, 1986–1987.

(6) Yuan, Q.; Yin, A.-X.; Luo, C.; Sun, L.-D.; Zhang, Y.-W.; Duan, W.-T.; Liu, H.-C.; Yan, C.-H. Facile Synthesis for Ordered Mesoporous γ-Aluminas with High Thermal Stability. *J. Am. Chem. Soc.* **2008**, *130*, 3465–3472.

(7) Cai, W.; Yu, J.; Anand, C.; Vinu, A.; Jaroniec, M. Facile Synthesis of Ordered Mesoporous Alumina and Alumina-Supported Metal Oxides with Tailored Adsorption and Framework Properties. *Chem. Mater.* **2011**, *23*, 1147–1157.

(8) Chen, C.; Ahn, W.-S. CO_2 Capture Using Mesoporous Alumina Prepared by a Sol–Gel Process. *Chem. Eng. J.* **2011**, *166*, 646–651.

(9) Cai, W.; Yu, J.; Cheng, B.; Su, B.-L.; Jaroniec, M. Synthesis of Boehmite Hollow Core/Shell and Hollow Microspheres via Sodium Tartrate-Mediated Phase Transformation and Their Enhanced Adsorption Performance in Water Treatment. *J. Phys. Chem. C* **2009**, *113*, 14739–14746.

(10) Li, W.; Cao, C.-Y.; Wu, L.-Y.; Ge, M.-F.; Song, W.-G. Superb Fluoride and Arsenic Removal Performance of Highly Ordered Mesoporous Aluminas. *J. Hazard. Mater.* **2011**, *198*, 143–150.

(11) Wei, J.; Ren, Y.; Luo, W.; Sun, Z.; Cheng, X.; Li, Y.; Deng, Y.; Elzatahry, A. A.; Al-Dahyan, D.; Zhao, D. Ordered Mesoporous Alumina with Ultra-Large Pores as an Efficient Absorbent for Selective Bioenrichment. *Chem. Mater.* **2017**, *29*, 2211–2217.

(12) Tan, K. W.; Moore, D. T.; Saliba, M.; Sai, H.; Estroff, L. A.; Hanrath, T.; Snaith, H. J.; Wiesner, U. Thermally Induced Structural Evolution and Performance of Mesoporous Block Copolymer-Directed Alumina Perovskite Solar Cells. *ACS Nano* **2014**, *8*, 4730–4739.

(13) Yang, X.; Cheng, X.; Song, H.; Ma, J.; Pan, P.; Elzatahry, A. A.; Su, J.; Deng, Y. 3D Interconnected Mesoporous Alumina with Loaded Hemoglobin as a Highly Active Electrochemical Biosensor for H_2O_2. *Adv. Healthcare Mater.* **2018**, *7*, 1800149.

(14) Zhang, Z.; Zhu, Y.; Asakura, H.; Zhang, B.; Zhang, J.; Zhou, M.; Han, Y.; Tanaka, T.; Wang, A.; Zhang, T.; Yan, N. Thermally Stable Single Atom Pt/m-Al_2O_3 for Selective Hydrogenation and CO Oxidation. *Nat. Commun.* **2017**, *8*, 16100.

(15) Tan, K. W.; Sai, H.; Robbins, S. W.; Werner, J. G.; Hoheisel, T. N.; Hesse, S. A.; Beaucage, P. A.; DiSalvo, F. J.; Gruner, S. M.; Murtagh, M.; Wiesner, U. Ordered Mesoporous Crystalline Aluminas from Self-Assembly of ABC Triblock Terpolymer–Butanol–Alumina Sols. *RSC Adv.* **2015**, *5*, 49287–49294.

(16) Patra, A. K.; Dutta, A.; Bhaumik, A. Self-Assembled Mesoporous γ-Al_2O_3 Spherical Nanoparticles and Their Efficiency for the Removal of Arsenic from Water. *J. Hazard. Mater.* **2012**, *201–202*, 170–177.
(17) Bhanja, P.; Kayal, U.; Bhaumik, A. Ordered Mesoporous γ-Al_2O_3 as Highly Efficient and Recyclable Catalyst for the Knoevenagel Reaction at Room Temperature. *Mol. Catal.* **2018**, *451*, 220–227.
(18) Kresge, C. T.; Leonowicz, M. E.; Roth, W. J.; Vartuli, J. C.; Beck, J. S. Ordered Mesoporous Molecular Sieves Synthesized by a Liquid-Crystal Template Mechanism. *Nature* **1992**, *359*, 710–712.
(19) Bagshaw, S. A.; Prouzet, E.; Pinnavaia, T. J. Templating of Mesoporous Molecular Sieves by Nonionic Polyethylene Oxide Surfactants. *Science* **1995**, *269*, 1242–1244.
(20) Templin, M.; Franck, A.; Chesne, A. D.; Leist, H.; Zhang, Y.; Ulrich, R.; Schädler, V.; Wiesner, U. Organically Modified Aluminosilicate Mesostructures from Block Copolymer Phases. *Science* **1997**, *278*, 1795–1798.
(21) Zhao, D.; Feng, J.; Huo, Q.; Melosh, N.; Fredrickson, G. H.; Chmelka, B. F.; Stucky, G. D. Triblock Copolymer Syntheses of Mesoporous Silica with Periodic 50 to 300 Angstrom Pores. *Science* **1998**, *279*, 548–552.
(22) Yang, P.; Zhao, D.; Margolese, D. I.; Chmelka, B. F.; Stucky, G. D. Generalized Syntheses of Large-Pore Mesoporous Metal Oxides with Semicrystalline Frameworks. *Nature* **1998**, *396*, 152–155.
(23) Li, Y.; Horia, R.; Tan, W. X.; Larbaram, N.; Sasangka, W. A.; Manalastas, W.; Madhavi, S.; Tan, K. W. Mesoporous Titanium Oxynitride Monoliths from Block Copolymer-Directed Self-Assembly of Metal–Urea Additives. *Langmuir* **2020**, *36*, 10803–10810.
(24) Meng, Y.; Gu, D.; Zhang, F.; Shi, Y.; Cheng, L.; Feng, D.; Wu, Z.; Chen, Z.; Wan, Y.; Stein, A.; Zhao, D. A Family of Highly Ordered Mesoporous Polymer Resin and Carbon Structures from Organic−organic Self-Assembly. *Chem. Mater.* **2006**, *18*, 4447–4464.
(25) Tan, K. W.; Jung, B.; Werner, J. G.; Rhoades, E. R.; Thompson, M. O.; Wiesner, U. Transient Laser Heating Induced Hierarchical Porous Structures from Block Copolymer–Directed Self-Assembly. *Science* **2015**, *349*, 54–58.
(26) Grant, S. M.; Vinu, A.; Pikus, S.; Jaroniec, M. Adsorption and Structural Properties of Ordered Mesoporous Alumina Synthesized in the Presence of F127 Block Copolymer. *Colloids Surf., A* **2011**, *385*, 121–125.
(27) Grant, S. M.; Jaroniec, M. Effect of Acid Concentration on Pore Size in Polymer - Templated Mesoporous Alumina. *J. Mater. Chem.* **2012**, *22*, 86–92.
(28) Wu, Z.; Li, Q.; Feng, D.; Webley, P. A.; Zhao, D. Ordered Mesoporous Crystalline γ-Al_2O_3 with Variable Architecture and Porosity from a Single Hard Template. *J. Am. Chem. Soc.* **2010**, *132*, 12042–12050.
(29) Dacquin, J.-P.; Dhainaut, J.; Duprez, D.; Royer, S.; Lee, A. F.; Wilson, K. An Efficient Route to Highly Organized, Tunable Macroporous−Mesoporous Alumina. *J. Am. Chem. Soc.* **2009**, *131*, 12896–12897.
(30) Ji, L.; Lin, J.; Tan, K. L.; Zeng, H. C. Synthesis of High-Surface-Area Alumina Using Aluminum Tri-*Sec*-Butoxide−2,4-Pentanedione−2-Propanol−Nitric Acid Precursors. *Chem. Mater.* **2000**, *12*, 931–939.
(31) Brunauer, S.; Emmett, P. H.; Teller, E. Adsorption of Gases in Multimolecular Layers. *J. Am. Chem. Soc.* **1938**, *60*, 309–319.

(32) Barrett, E. P.; Joyner, L. G.; Halenda, P. P. The Determination of Pore Volume and Area Distributions in Porous Substances. I. Computations from Nitrogen Isotherms. *J. Am. Chem. Soc.* **1951**, *73*, 373–380.
(33) Kruk, M.; Jaroniec, M.; Sayari, A. Application of Large Pore MCM-41 Molecular Sieves to Improve Pore Size Analysis Using Nitrogen Adsorption Measurements. *Langmuir* **1997**, *13*, 6267–6273.
(34) Lippens, B. C.; de Boer, J. H. Studies on Pore Systems in Catalysts: V. The *t* Method. *J. Catal.* **1965**, *4*, 319–323.
(35) Pérez, L. L.; Perdriau, S.; Brink, G. ten; Kooi, B. J.; Heeres, H. J.; Melián-Cabrera, I. Stabilization of Self-Assembled Alumina Mesophases. *Chem. Mater.* **2013**, *25*, 848–855.
(36) Wu, Q.; Zhang, F.; Yang, J.; Li, Q.; Tu, B.; Zhao, D. Synthesis of Ordered Mesoporous Alumina with Large Pore Sizes and Hierarchical Structure. *Microporous Mesoporous Mater.* **2011**, *143*, 406–412.
(37) Fan, J.; Boettcher, S. W.; Stucky, G. D. Nanoparticle Assembly of Ordered Multicomponent Mesostructured Metal Oxides via a Versatile Sol−Gel Process. *Chem. Mater.* **2006**, *18*, 6391–6396.
(38) Crepaldi, E. L.; Soler-Illia, G. J. de A. A.; Grosso, D.; Cagnol, F.; Ribot, F.; Sanchez, C. Controlled Formation of Highly Organized Mesoporous Titania Thin Films: From Mesostructured Hybrids to Mesoporous Nanoanatase TiO_2. *J. Am. Chem. Soc.* **2003**, *125*, 9770–9786.
(39) Stefik, M.; Song, J.; Sai, H.; Guldin, S.; Boldrighini, P.; Orilall, M. C.; Steiner, U.; Gruner, S. M.; Wiesner, U. Ordered Mesoporous Titania from Highly Amphiphilic Block Copolymers: Tuned Solution Conditions Enable Highly Ordered Morphologies and Ultra-Large Mesopores. *J. Mater. Chem. A* **2015**, *3*, 11478–11492.
(40) Garcia, B. C.; Kamperman, M.; Ulrich, R.; Jain, A.; Gruner, S. M.; Wiesner, U. Morphology Diagram of a Diblock Copolymer−Aluminosilicate Nanoparticle System. *Chem. Mater.* **2009**, *21*, 5397–5405.
(41) Hudson, S.; Tanner, D. A.; Redington, W.; Magner, E.; Hodnett, K.; Nakahara, S. Quantitative TEM Analysis of a Hexagonal Mesoporous Silicate Structure. *Phys. Chem. Chem. Phys.* **2006**, *8*, 3467–3474.
(42) Israelachvili, J. N. *Intermolecular and Surface Forces*, 3rd Ed.; Academic Press: Burlington, MA, 2011.
(43) Tolbert, S. H.; Landry, C. C.; Stucky, G. D.; Chmelka, B. F.; Norby, P.; Hanson, J. C.; Monnier, A. Phase Transitions in Mesostructured Silica/Surfactant Composites: Surfactant Packing and the Role of Charge Density Matching. *Chem. Mater.* **2001**, *13*, 2247–2256.
(44) Kunz, W.; Testard, F.; Zemb, T. Correspondence between Curvature, Packing Parameter, and Hydrophilic−Lipophilic Deviation Scales around the Phase-Inversion Temperature. *Langmuir* **2009**, *25*, 112–115.
(45) Sai, H.; Tan, K. W.; Hur, K.; Asenath-Smith, E.; Hovden, R.; Jiang, Y.; Riccio, M.; Muller, D. A.; Elser, V.; Estroff, L. A.; Gruner, S. M.; Wiesner, U. Hierarchical Porous Polymer Scaffolds from Block Copolymers. *Science* **2013**, *341*, 530–534.
(46) Jo, C.; Hwang, J.; Lim, W.-G.; Lim, J.; Hur, K.; Lee, J. Multiscale Phase Separations for Hierarchically Ordered Macro/Mesostructured Metal Oxides. *Adv. Mater.* **2018**, *30*, 1703829.

(47) Hwang, J.; Jo, C.; Hur, K.; Lim, J.; Kim, S.; Lee, J. Direct Access to Hierarchically Porous Inorganic Oxide Materials with Three-Dimensionally Interconnected Networks. *J. Am. Chem. Soc.* **2014**, *136*, 16066–16072.
(48) Tokudome, Y.; Fujita, K.; Nakanishi, K.; Miura, K.; Hirao, K. Synthesis of Monolithic Al_2O_3 with Well-Defined Macropores and Mesostructured Skeletons via the Sol−Gel Process Accompanied by Phase Separation. *Chem. Mater.* **2007**, *19*, 3393–3398.
(49) Hasegawa, G.; Kanamori, K.; Kiyomura, T.; Kurata, H.; Abe, T.; Nakanishi, K. Hierarchically Porous Carbon Monoliths Comprising Ordered Mesoporous Nanorod Assemblies for High-Voltage Aqueous Supercapacitors. *Chem. Mater.* **2016**, *28*, 3944–3950.
(50) Baute, D.; Goldfarb, D. Interaction of Nitrates with Pluronic Micelles and Their Role in the Phase Formation of Mesoporous Materials. *J. Phys. Chem. C* **2007**, *111*, 10931–10940.
(51) Warren, S. C.; DiSalvo, F. J.; Wiesner, U. Nanoparticle-Tuned Assembly and Disassembly of Mesostructured Silica Hybrids. *Nat. Mater.* **2007**, *6*, 156–161.
(52) Thompson, R. B.; Ginzburg, V. V.; Matsen, M. W.; Balazs, A. C. Predicting the Mesophases of Copolymer-Nanoparticle Composites. *Science* **2001**, *292*, 2469–2472.
(53) Brinker, C. J. *Sol-Gel Science: The Physics and Chemistry of Sol-Gel Processing*; Academic Press: Boston, 1990.
(54) Mohsen-Nia, M.; Amiri, H.; Jazi, B. Dielectric Constants of Water, Methanol, Ethanol, Butanol and Acetone: Measurement and Computational Study. *J. Solution Chem.* **2010**, *39*, 701–708.
(55) Pérez, L. L.; Zarubina, V.; Heeres, H. J.; Melián-Cabrera, I. Condensation-Enhanced Self-Assembly as a Route to High Surface Area α-Aluminas. *Chem. Mater.* **2013**, *25*, 3971–3978.
(56) Sevilla, M.; Fuertes, A. B. Sustainable Porous Carbons with a Superior Performance for CO_2 Capture. *Energy Environ. Sci.* **2011**, *4*, 1765–1771.
(57) Oschatz, M.; Antonietti, M. A Search for Selectivity to Enable CO_2 Capture with Porous Adsorbents. *Energy Environ. Sci.* **2018**, *11*, 57–70.
(58) Singh, G.; Lee, J.; Karakoti, A.; Bahadur, R.; Yi, J.; Zhao, D.; AlBahily, K.; Vinu, A. Emerging Trends in Porous Materials for CO_2 Capture and Conversion. *Chem. Soc. Rev.* **2020**, *49*, 4360–4404.
(59) Zhang, G.; Zhao, P.; Hao, L.; Xu, Y. Amine-Modified SBA-15(P): A Promising Adsorbent for CO_2 Capture. *J. CO_2 Util.* **2018**, *24*, 22–33.
(60) Mason, J. A.; McDonald, T. M.; Bae, T.-H.; Bachman, J. E.; Sumida, K.; Dutton, J. J.; Kaye, S. S.; Long, J. R. Application of a High-Throughput Analyzer in Evaluating Solid Adsorbents for Post-Combustion Carbon Capture via Multicomponent Adsorption of CO_2, N_2, and H_2O. *J. Am. Chem. Soc.* **2015**, *137*, 4787–4803.
(61) Estevez, L.; Barpaga, D.; Zheng, J.; Sabale, S.; Patel, R. L.; Zhang, J.-G.; McGrail, B. P.; Motkuri, R. K. Hierarchically Porous Carbon Materials for CO_2 Capture: The Role of Pore Structure. *Ind. Eng. Chem. Res.* **2018**, *57*, 1262–1268.
(62) Ho, Y. S.; McKay, G. Pseudo-Second Order Model for Sorption Processes. *Process Biochem.* **1999**, *34*, 451–465.

Graphical Table of Contents

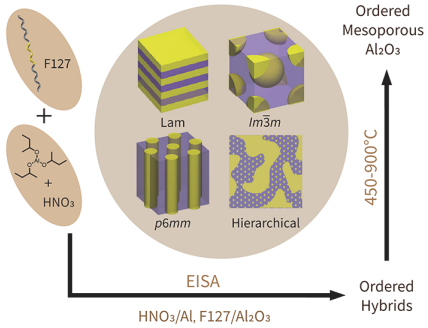

Supporting Information

Ordered Mesoporous Alumina with Tunable Morphologies and Pore Sizes for CO_2 Capture and Dye Separation

Geok Leng Seah,[†,⊥] Leyan Wang,[†,⊥] Li Fang Tan,[†] Chanikarn Tipjanrawee,[†] Wardhana A. Sasangka,[†] Adam K. Usadi,[‡] Jonathan M. McConnachie,[‡] and Kwan W. Tan[†,]*

[†]School of Materials Science and Engineering, Nanyang Technological University, Singapore 639798, Singapore.

[‡]ExxonMobil Research and Engineering Company, Annandale, New Jersey 08801, United States.

[⊥]These authors contributed equally to the work.

[*]Address correspondence to kwtan@ntu.edu.sg.

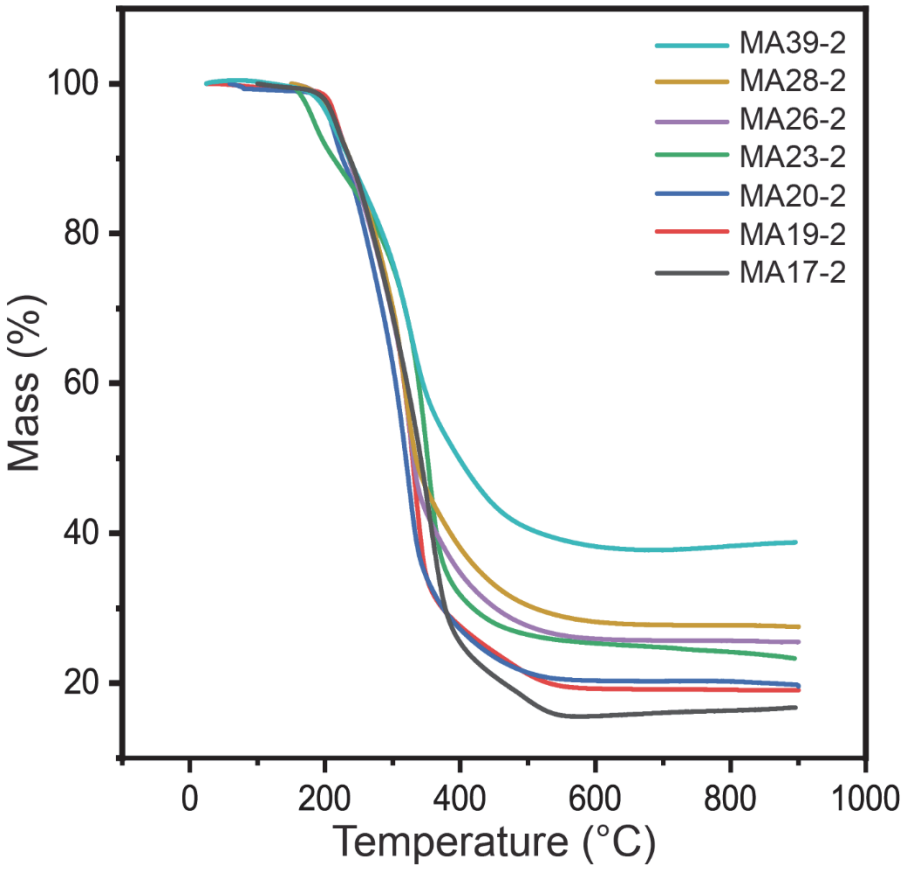

Figure S1. TGA data for MA17-2 to MA39-2 hybrid samples.

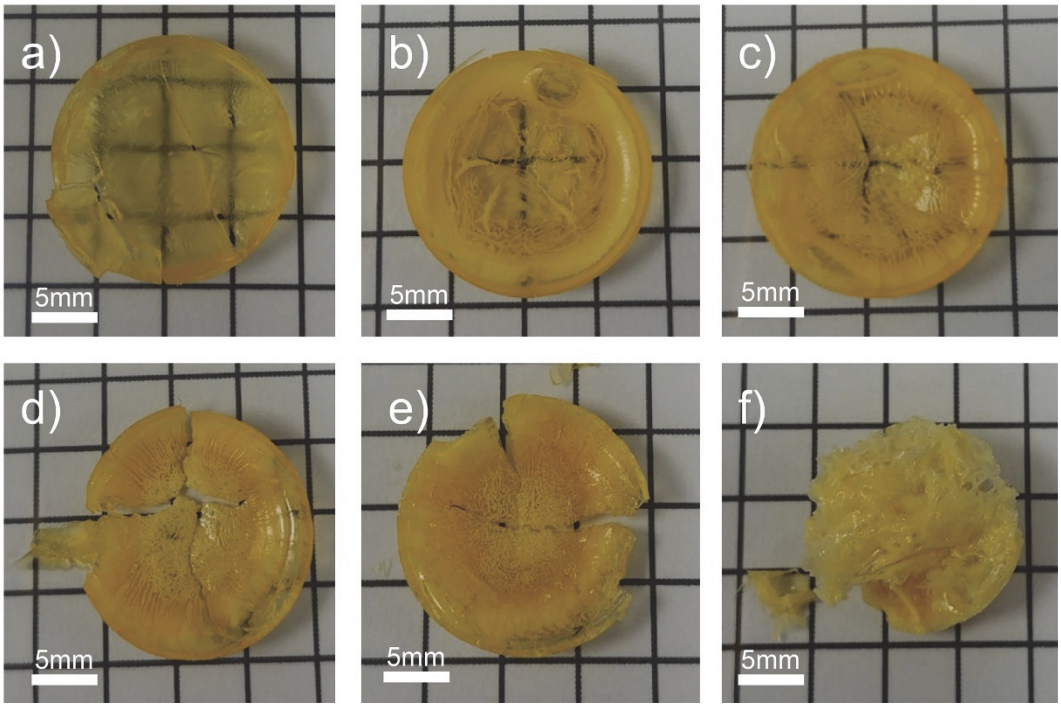

Figure S2. Optical images of F127–Al_2O_3 hybrid monoliths of (a) MA17-2, (b) MA19-2, (c) MA20-2, (d) MA23-2, (e) MA26-2 and (f) MA39-2.

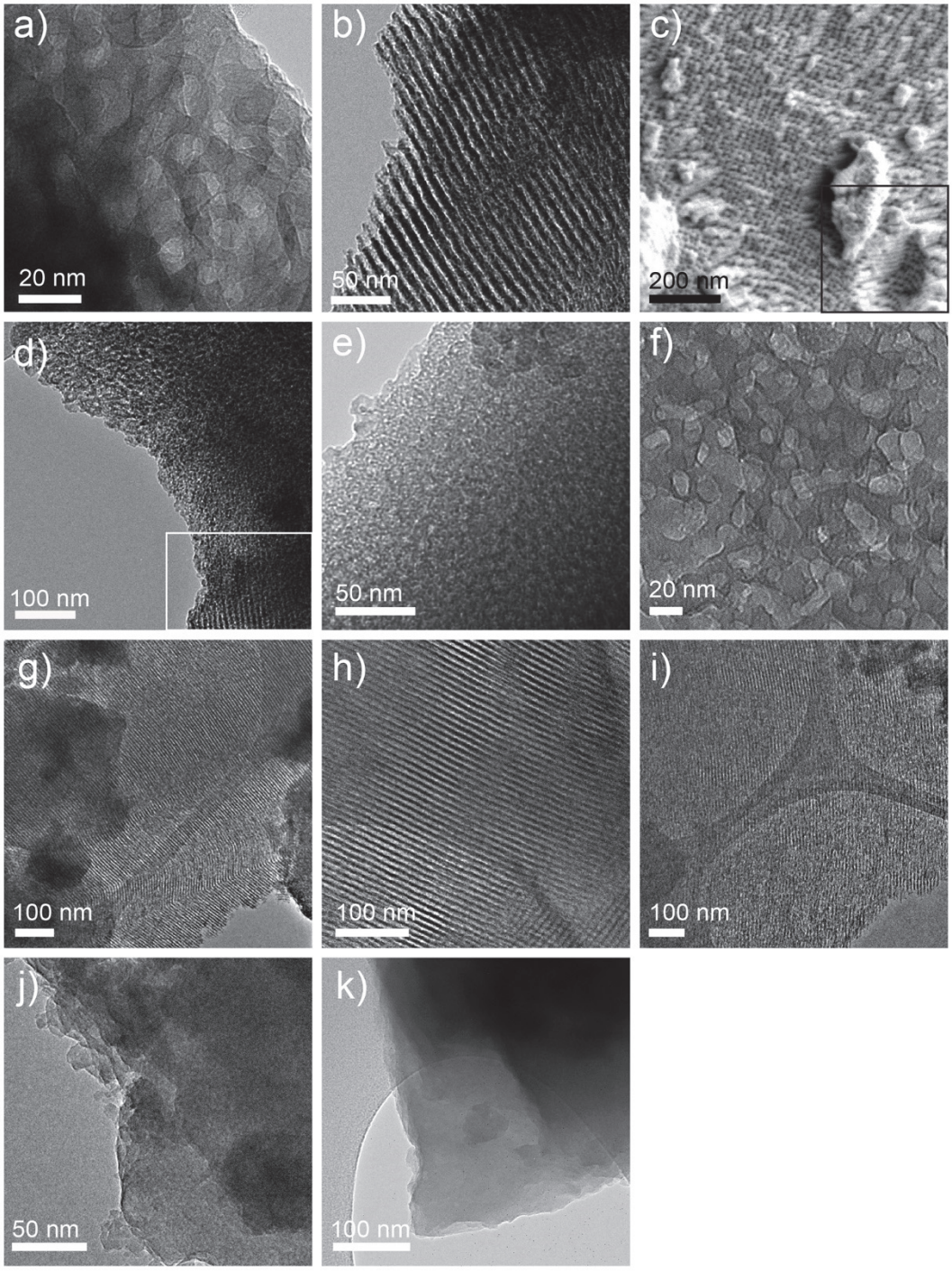

Figure S3. TEM/SEM micrographs of (a) wormlike structures of MA17-2-450, (b) hexagonal cylinders of MA19-2-450, (c) hexagonal and cubic structures of MA26-2-450, (d) hexagonal and wormlike structures of MA26-2-450, (e) wormlike structures of MA28-2-450, (f) wormlike structures of MA39-2-450, (g) hexagonal cylinders of MA23-1.8-450, (h) hexagonal cylinders of MA23-1.6-450, (i,j) biphasic hexagonal (i) and lamellar (j) structures of MA23-1.4-450, as well as (k) lamellar structure of MA23-1.2-450. The highlighted regions denoted in (c) and (d) show the hexagonal cylinder morphology.

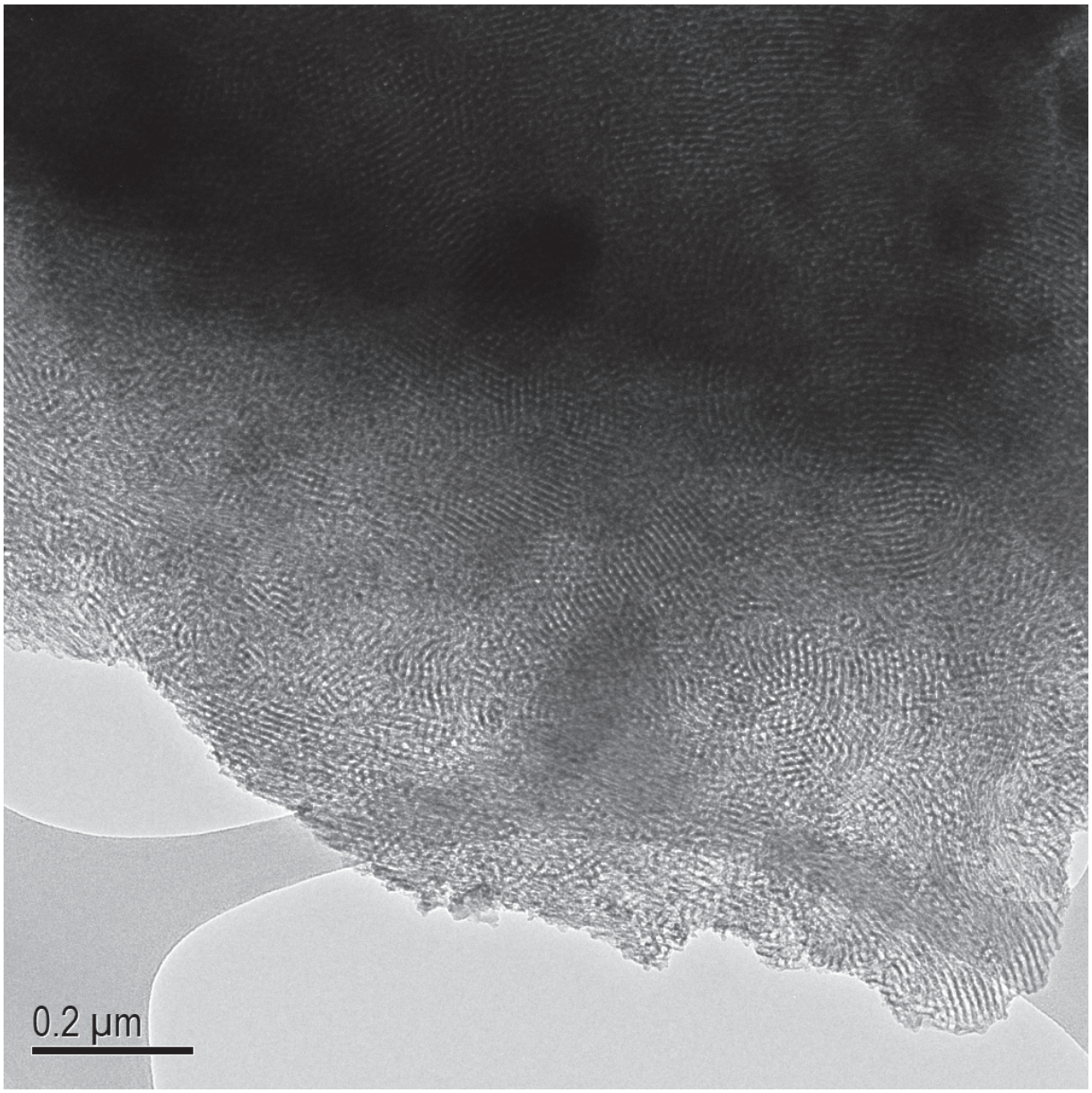

Figure S4. TEM micrograph of mesoporous MA20-2-450 showing biphasic hexagonal and cubic morphologies.

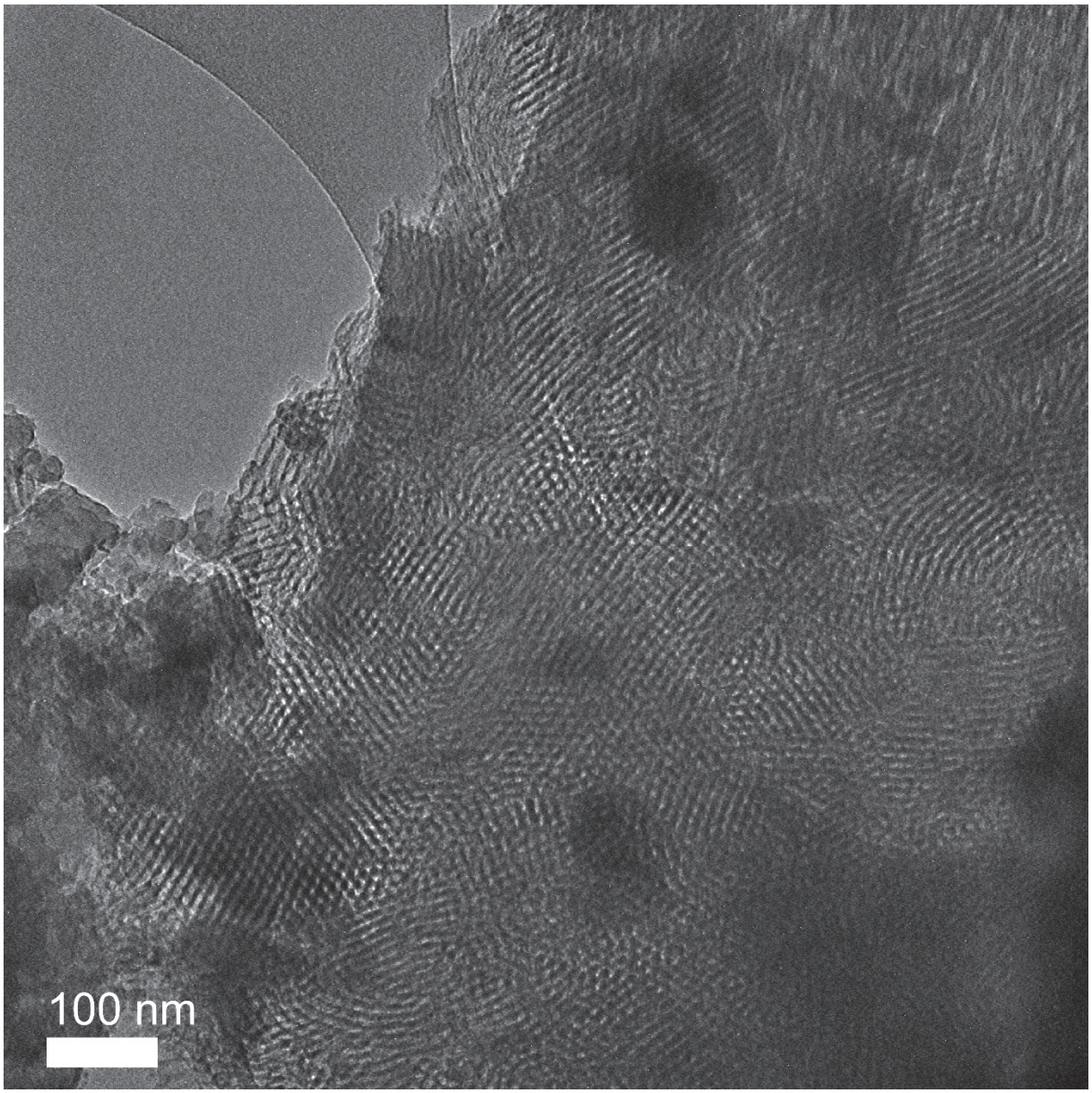

Figure S5. TEM micrograph of mesoporous MA23-2-450 showing biphasic hexagonal and cubic morphologies.

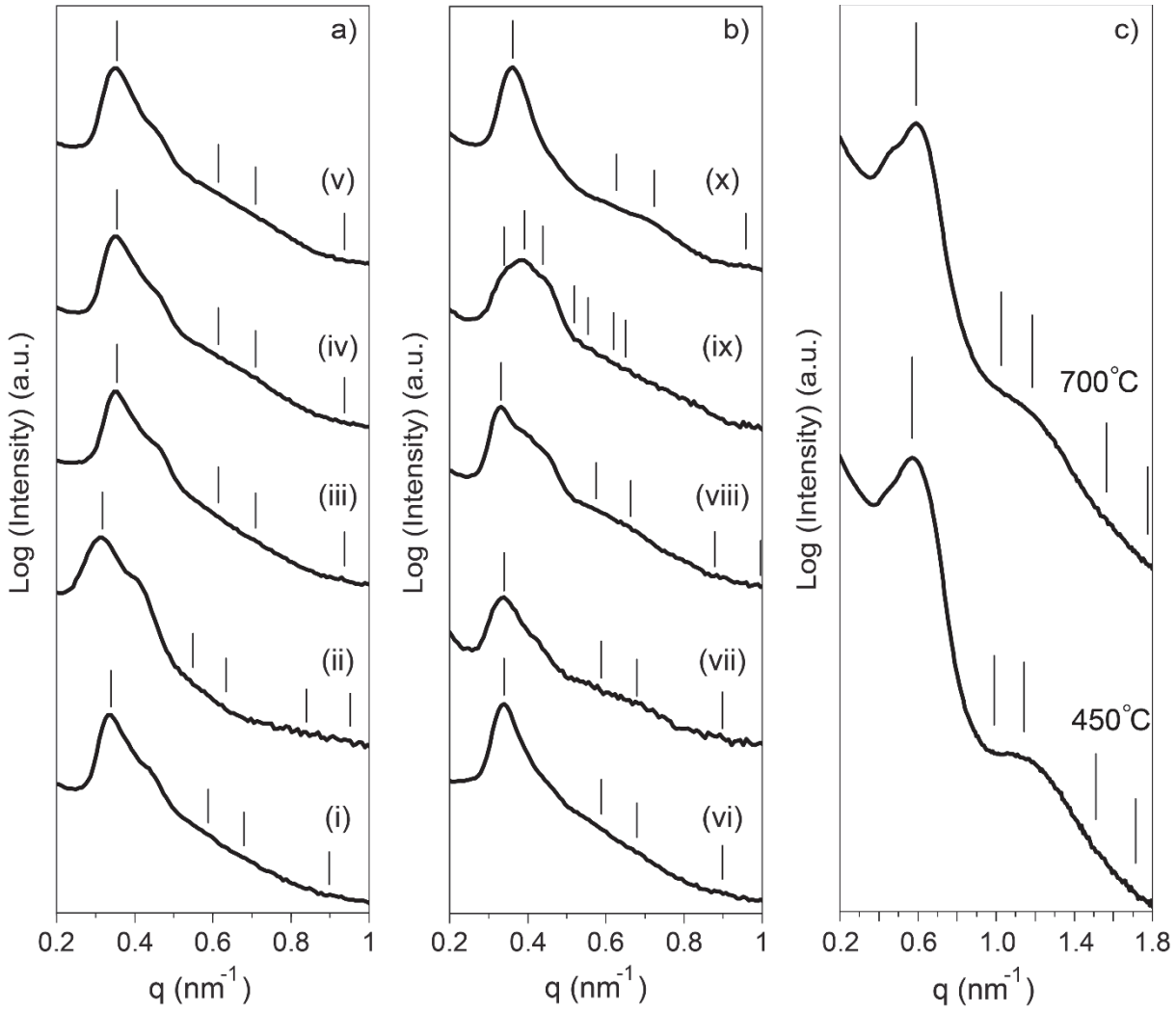

Figure S6. SAXS patterns of (a,b) ten other hybrid samples of MA28-2 and (c) MA28-2-450 and MA28-2-700 as indicated.

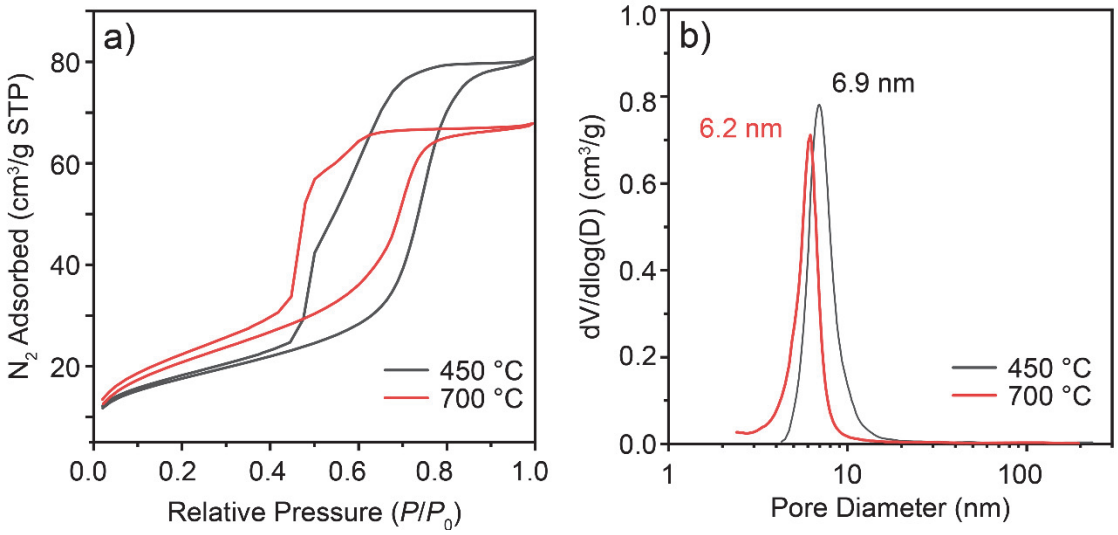

Figure S7. (a) Nitrogen sorption isotherms and (b) pore size distributions of MA28-2-450 and MA28-2-700 as indicated.

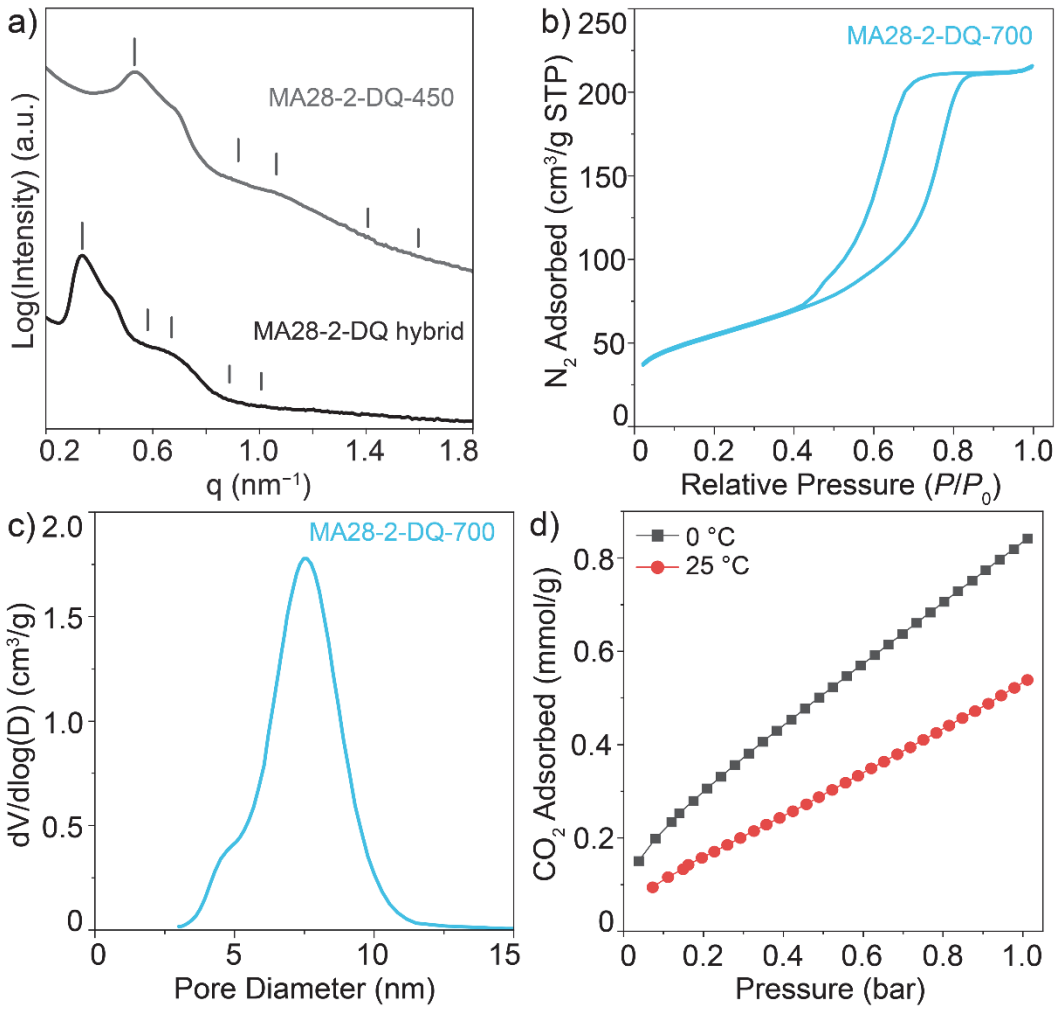

Figure S8. (a) Integrated SAXS patterns of MA28-2-DQ hybrid (black) formed at a faster solvent evaporation rate resulting a deeper quench depth, as well as MA28-2-DQ-450 (gray) after annealing at 450 °C. (b) Nitrogen sorption isotherm and (c) pore size distribution, as well as (d) CO_2 adsorption isotherms at 0 °C and 25 °C, of MA28-2-DQ-700.

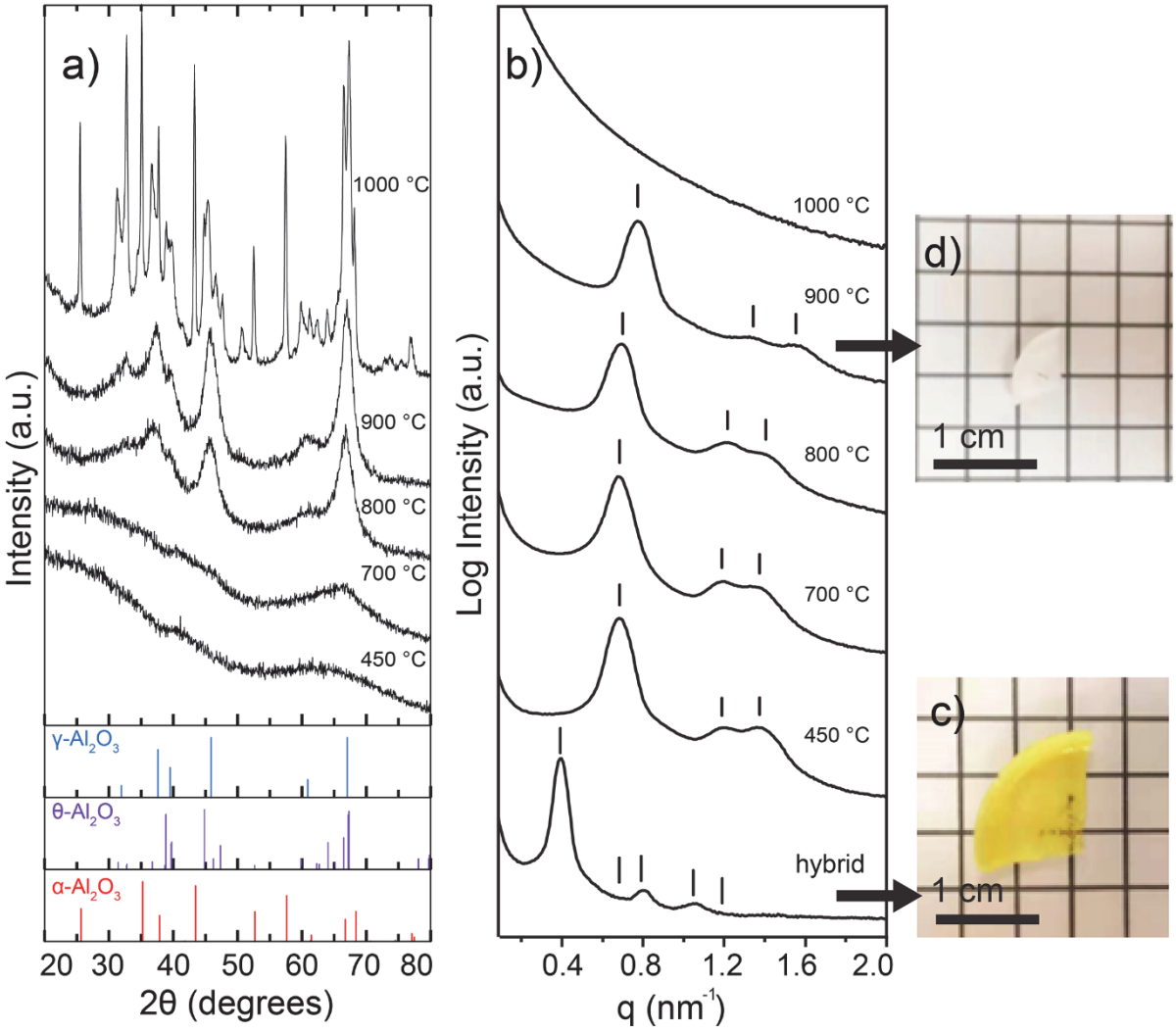

Figure S9. (a) PXRD and (b) SAXS patterns of mesoporous MA23-1.6 samples thermally annealed in air at 450–1000 °C. The PXRD peak markings and relative intensities for γ-Al_2O_3 (blue, PDF 00-010-0425), θ-Al_2O_3 (purple, PDF 00-056-0456) and α-Al_2O_3 (red, PDF 04-004-2852) are shown in (a). (c,d) Optical images of (c) MA23-1.6 hybrid and (d) MA23-1.6-900.

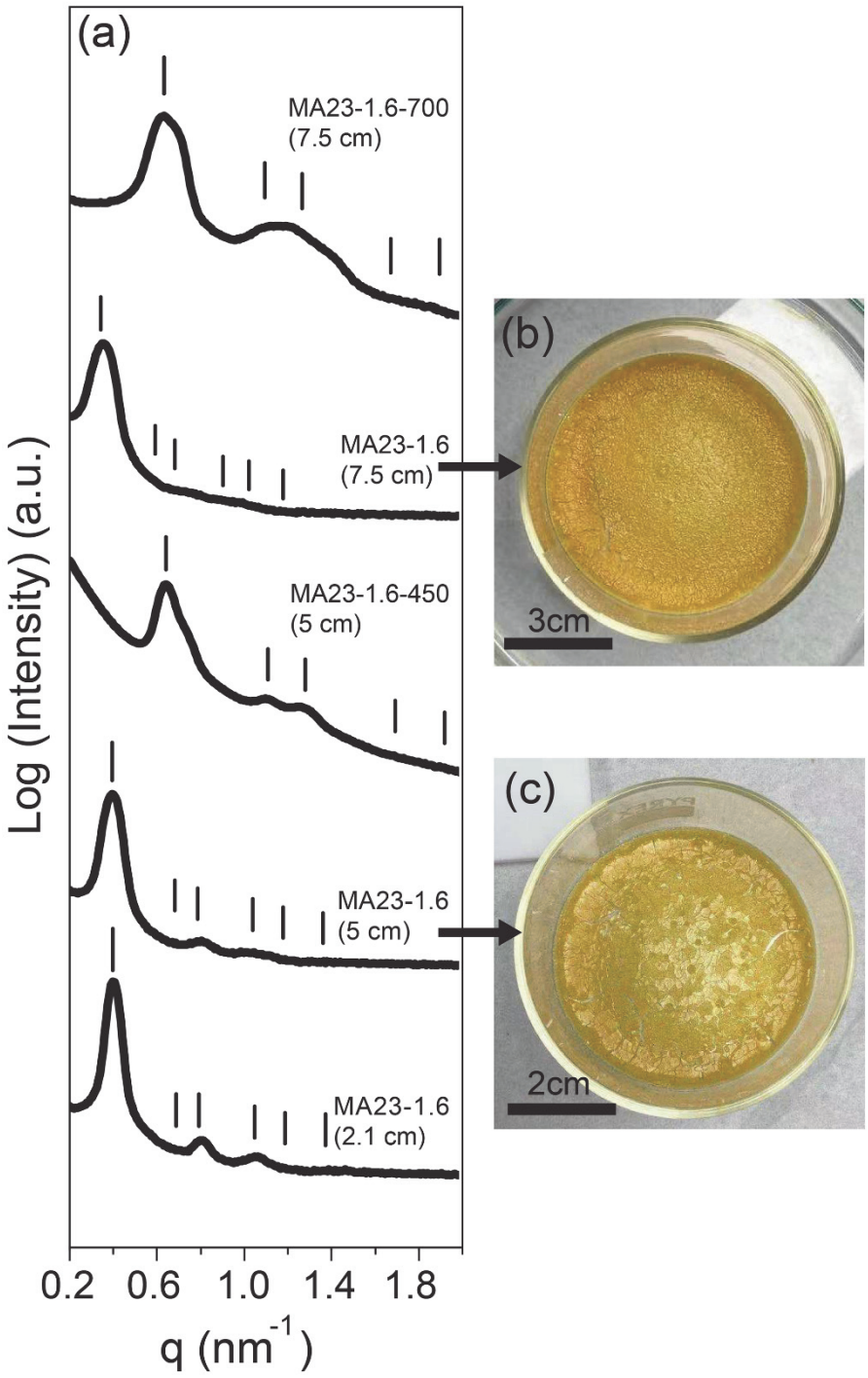

Figure S10. (a) SAXS patterns of MA23-1.6 hybrids, MA23-1.6-450 and MA23-1.6-700 samples (b,c) Optical images of MA23-1.6 hybrids prepared in crystallization dishes of diameter 7.5 cm (b) and 5 cm (c).

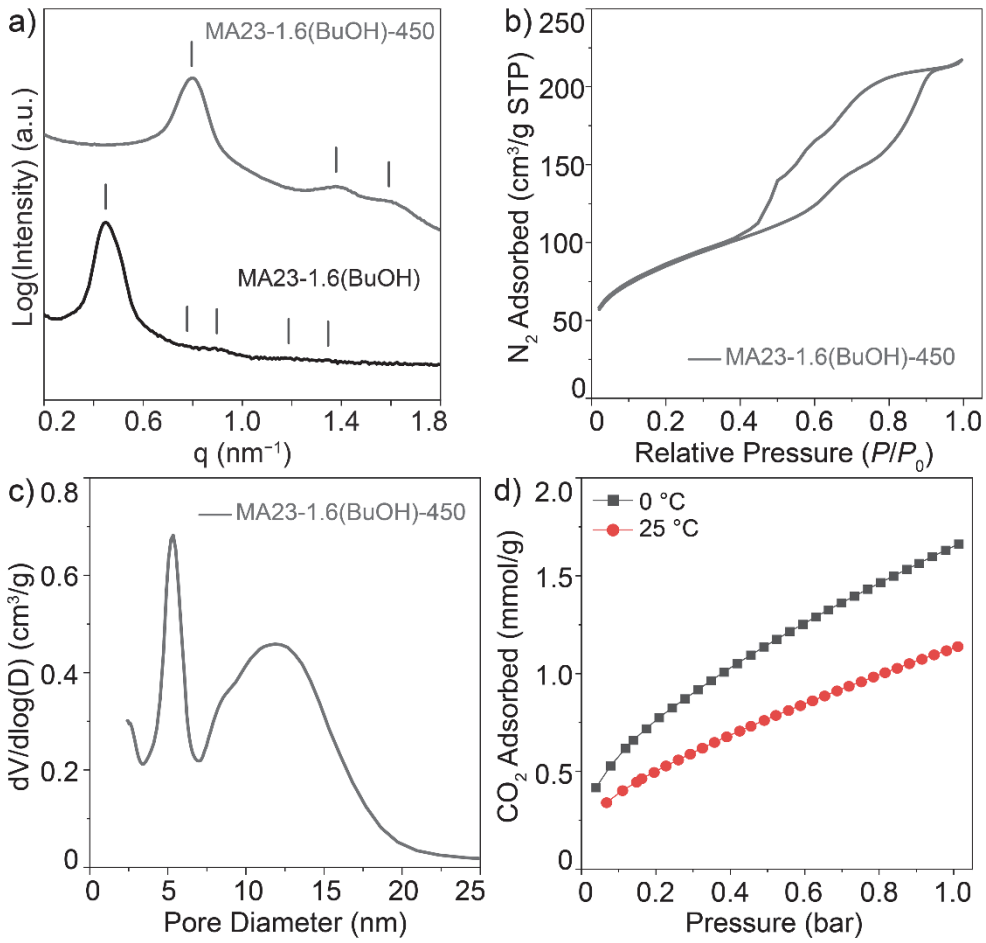

Figure S11. (a) Integrated SAXS patterns of *n*-BuOH derived MA23-1.6(BuOH) hybrid (black) and MA23-1.6(BuOH)-450 (gray). (b) Nitrogen sorption isotherm and (c) pore size distribution, as well as (d) CO_2 adsorption isotherms at 0 °C and 25 °C, of MA23-1.6(BuOH)-450.

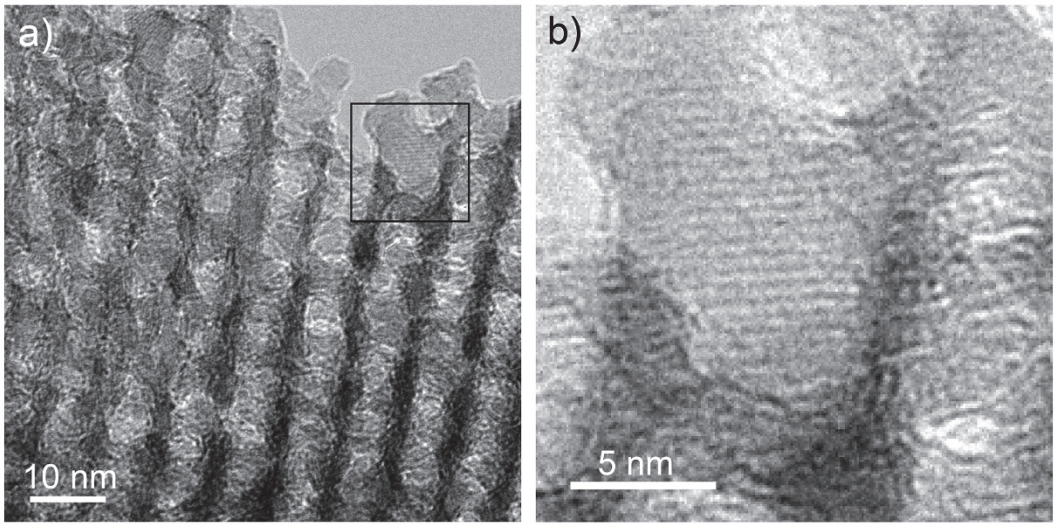

Figure S12. (a, b) HR-TEM images suggest network-like structures in MA23-2-900. Panel (b) shows a higher magnification of the highlighted region in (a).

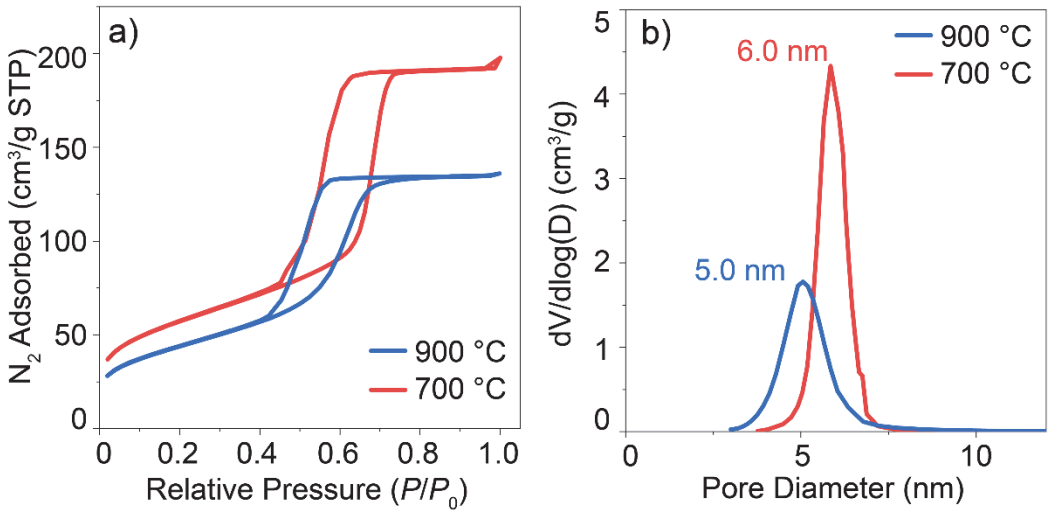

Figure S13. (a) Nitrogen sorption isotherm and (b) pore size distribution of MA23-1.6-700 and MA-1.6-900.

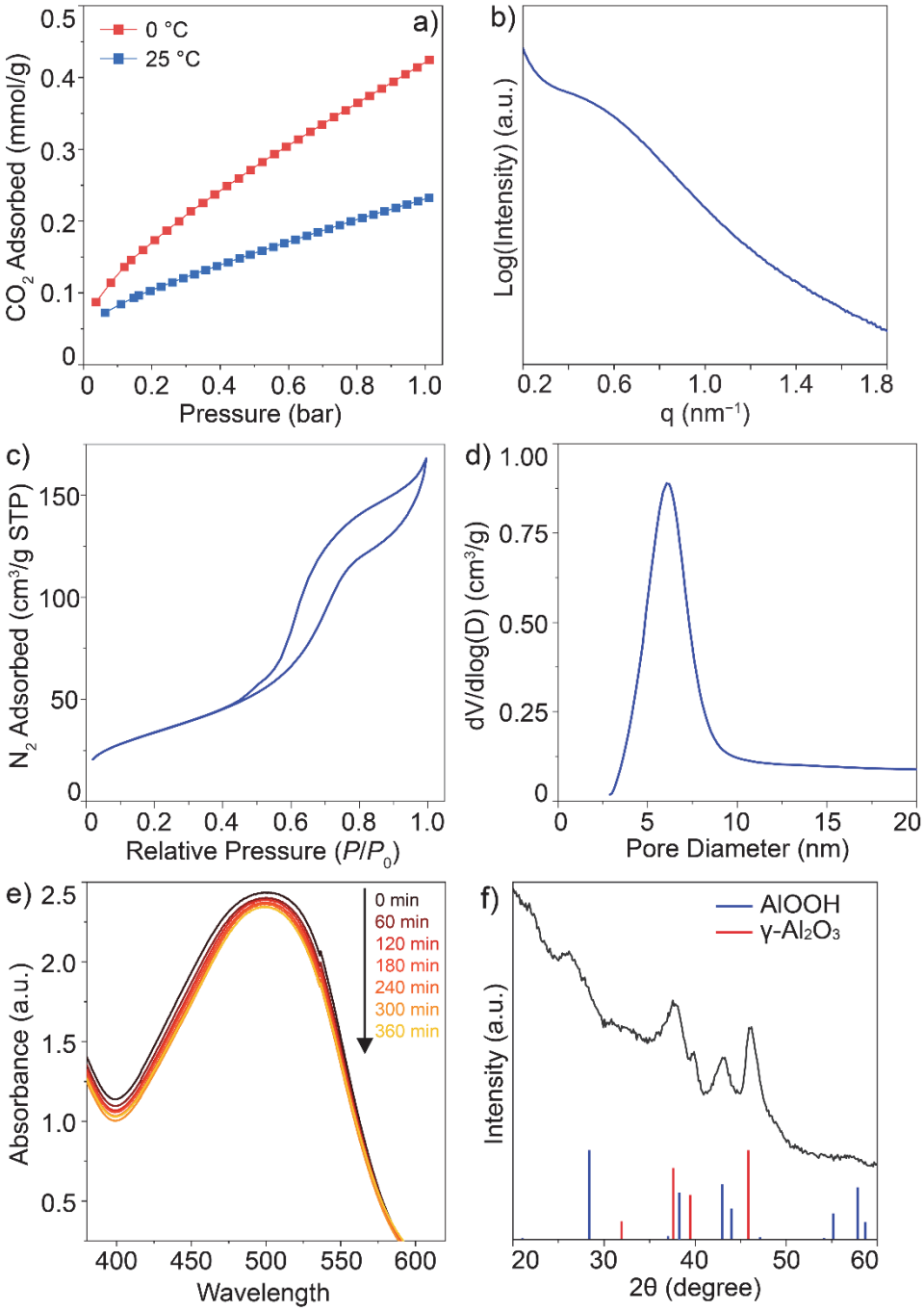

Figure S14. Plots of (a) CO_2 adsorption isotherms at 0 °C and 25 °C, (b) SAXS, (c) nitrogen sorption isotherm and (d) pore size distribution of commercial Al_2O_3. SAXS pattern in (b) indicates the commercial sample is mesoscopically disordered. (e) Absorbance spectra of Congo red aqueous solution after treatment with commercial Al_2O_3 at different time points as indicated. (f) WAXS of commercial Al_2O_3 with peak markings and relative intensities for γ-Al_2O_3 (red, PDF 00-010-0425) and AlOOH (blue, PDF 04-013-4266).